Modeling urban pollutant transport at multi-resolutions: Impacts of turbulent mixing

Zining Yang[1], Qiuyan Du[1], Qike Yang[1], Chun Zhao[1,2,3*], Gudongze Li[1], Zihan Xia[1], Mingyue Xu[1], Renmin Yuan[1], Yubin Li[4], Kaihui Xia[1], Jun Gu[1], and Jiawang Feng[1]

[1]Deep Space Exploration Laboratory/School of Earth and Space Sciences/CMA-USTC Laboratory of Fengyun Remote Sensing/State Key Laboratory of Fire Science/Institute of Advanced Interdisciplinary Research on High-Performance Computing Systems and Software, University of Science and Technology of China, Hefei, China

[2]Laoshan Laboratory, Qingdao, China

[3]CAS Center for Excellence in Comparative Planetology, University of Science and Technology of China, Hefei, China.

[4]School of Atmospheric Physics, Nanjing University of Information Science and Technology, Nanjing, China

*Corresponding author: Chun Zhao (chunzhao@ustc.edu.cn)

Key Points:

1. Higher horizontal resolutions improve BC surface concentration predictions by enhancing PBL mixing and vertical wind flux, especially at night.

2. Small-scale eddies resolved at higher horizontal resolutions strengthen vertical fluxes, increasing BC atmospheric lifetime and column concentrations.

3. **Detailed land use and terrain in high horizontal resolution models enhance PBL mixing, refining pollutant transport and urban air quality simulations.**

Abstract

Air pollution in cities impacts public health and climate. Turbulent mixing is crucial in pollutant formation and dissipation, yet current atmospheric models struggle to accurately represent it. Turbulent mixing intensity varies with model resolution, which has rarely been analyzed. To investigate turbulent mixing variations at multi-resolutions and their implications for urban pollutant transport, we conducted experiments using WRF-Chem at 25, 5, and 1 km resolutions. The simulated meteorological fields and black carbon (BC) concentrations are compared with observations. Differences in turbulent mixing across multi-resolutions are more pronounced at night, resulting in noticeable variations in BC concentrations. BC surface concentrations decrease as resolution increases from 25 km to 5 km and further to 1 km, but are similar at 5 km and 1 km resolutions. Enhanced planetary boundary layer (PBL) mixing coefficients and vertical wind flux at higher resolutions reduce BC surface concentration overestimations. The 1 km resolution parameterized lower mixing coefficients than 5 km but resolved more small-scale eddies, leading to similar near-surface turbulent mixing at both resolutions, while the intensity at higher altitudes is greater at 1 km. This caused BC to be transported higher and farther, increasing its atmospheric lifetime and column concentrations. Variations in mixing coefficients are partly attributed to differences in land use and terrain, with higher resolutions providing more detailed information that enhances PBL mixing coefficients, while grid size remains crucial in regions with more gradual terrain and land use changes. This study interprets how turbulent mixing affects simulated urban pollutant diffusion at multi-resolutions.

1. Introduction

Since the middle of the 19th century, rapid economic growth and urbanization have caused severe regional haze and photochemical smog pollution (Li et al., 2015; Li et al., 2019; Ma et al., 2019). A variety of air pollution episodes mainly occur in cities (Chan and Yao, 2008). Exposure to atmospheric particulate matter is one of the major threats to public health (Yin et al., 2017; Liu et al., 2019). Accurate pollutant estimation is crucial for the realization of pollution prevention goals. Pollution processes are affected by many different factors, such as pollution source emissions (Li et al., 2017a), physical and chemical characteristics of aerosols (Riccobono et al., 2014; Zhao et al., 2018), topographic effects (Zhang et al., 2018), and meteorological conditions (Ye et al., 2016). Significantly, pollutant concentrations are mainly gathered within the planetary boundary layer (PBL), and PBL mixing processes are associated with intricate turbulent eddies (Stull, 1988), which significantly affect the horizontal transport and vertical diffusion of pollutants (Wang et al., 2018; Du et al., 2020; Ren et al., 2020; Ren et al., 2021), as well as the formation of new aerosol particles (Wu et al., 2021).

The mechanism of turbulent transport has been widely investigated. The vertical diffusion of pollutants in urban areas is affected by the structure of the urban boundary layer (UBL), and different structures may lead to uneven spatial distribution of pollutants (Han et al., 2009; Zhao et al., 2013c). First, meteorological conditions play dominant roles in turbulent mixing of air pollutants within the atmospheric boundary layer (ABL) (Xu et al., 2015; Miao et al., 2019). Unstable meteorological conditions enhance turbulence, promoting pollutant dispersion, while stable conditions suppress it, leading to pollutants accumulation. Previous studies have indicated that constant stagnant winds and increased water vapor density inhibit the vertical diffusion of pollutants, resulting in explosive growth of pollutants (Zhang et al., 2015a; Zhang et al., 2015b; Wei et al., 2018; Zhong et al., 2018). Under these stable conditions, the inherent characteristics of the stable boundary layer (SBL), particularly turbulence intermittency (Costa et al., 2011), affect the heavy urban haze events by altering surface-atmosphere exchanges (Wei et al., 2018; Ren et al., 2019a; Ren et al., 2019b; Wei et al., 2020; Ren

86   et al., 2021; Zhang et al., 2022). Second, diurnal variations in turbulent mixing between

87   day and night significantly influence changes in pollutant concentrations (Li et al., 2018;

88   Liu et al., 2020). In the daytime convective boundary layer (CBL), pollutants can be

89   mixed uniformly in a thick layer due to the intense turbulent mixing (Sun et al., 2018).

90   While in the nighttime SBL, reduced mixing and dispersion result in the accumulation

91   of pollutants near the surface (Holmes et al., 2015). Severe urban haze pollution

92   formation is typically accompanied with the development of nocturnal SBL (Pierce et

93   al., 2019; Li et al., 2020; Zhang et al., 2020; Li et al., 2022). Moreover, pollutants in

94   the residual layer can be mixed downward to the surface with the development of the

95   ABL the next morning (Chen et al., 2009; Sun et al., 2013; Quan et al., 2020). Overall,

96   the impact of turbulent mixing on urban pollution is important and complex.

97   Numerical simulation is an important method for studying turbulent mixing.

98   However, there are still challenges associated with accurately representing turbulent

99   mixing in numerical models. Previous research has indicated that turbulent mixing in

100   current atmospheric chemical models is insufficient to capture stable atmospheric

101   conditions, potentially leading to rapid increases in severe haze in urban areas (Wang

102   et al., 2018; Peng et al., 2018; Ren et al., 2019b; Du et al., 2020). Some studies revealed

103   that WRF-Chem simulations underestimate turbulent exchange within stable nocturnal

104   boundary layers, allowing unrealistic accumulation of pollutants near the surface

105   (Tuccella et al., 2012; Berger et al., 2016). Additionally, PBL parameterization schemes

106   in current models may not accurately represent intricate turbulent mixing, particularly

107   in complex terrains, urban areas, or extreme weather conditions. Research has revealed

108   that different PBL parameterization schemes employed in WRF-Chem tend to

109   underestimate turbulent mixing when compared to observations (Hong et al., 2006;

110   Banks and Baldasano, 2016; Kim, 2006). Turbulent mixing coefficients diagnosed in

111   atmospheric models characterize the intensity of turbulent mixing (Cuchiara et al.,

112   2014). However, these models frequently underestimate mixing coefficients during the

113   nighttime. Previous research has employed various approaches to address this

114   limitation. Du et al. (2020) demonstrated that increasing the lower limit of PBL mixing

115   coefficients during nighttime significantly reduced the modeling biases in simulated

pollutant concentrations. Jia and Zhang (2021) utilized the new modified turbulent diffusion coefficient to represent the mixing process of pollutants separately and improved the simulation results of pollutant concentrations. Jia et al. (2021) employed the revised turbulent mixing coefficient of particles using high-resolution vertical flux data of particles according to the mixing length theory, and improved the overestimation of pollutant concentrations. In conclusion, current atmospheric models commonly face several challenges in accurately simulating turbulent mixing.

The representation of turbulent mixing in models is influenced by various factors, including grid resolution, topography, boundary layer parameterization, atmospheric dynamics, and land-surface processes. Among these factors, model resolution can significantly affect turbulent mixing processes in atmospheric simulations, with simulated turbulent mixing varying substantially across different resolutions. Qian et al. (2010) evaluated model performance at 3 km, 15 km, and 75 km resolutions, finding that only simulations at 3 km resolution accurately captured multiple concentration peaks in observational data, indicating that turbulent mixing may play a critical role in simulating pollutant concentrations. Fountoukis et al. (2013) conducted model simulations at three resolutions and demonstrated that higher resolution reduced the bias for BC concentration by more than 30% in the Northeastern United States during winter, attributing this improvement to better resolved pollutant dispersion. Tao et al. (2020) found that changes in model resolution led to increased pollutant concentrations in urban areas but decreased concentrations in west mountain regions, likely due to differences in vertical and horizontal dispersion. In conclusion, previous research has primarily focused on comparing pollutant concentrations across different model resolutions, demonstrating that resolution significantly affects pollutant distribution and dispersion. These studies suggest that turbulent mixing may play a crucial role. However, few have systematically explored the specific mechanisms by which turbulent mixing influences pollutant concentrations simulated at multi-resolutions, despite their importance in determining urban atmospheric pollutions.

Motivated by aforementioned problems, this study aims to investigate differences in pollutant concentrations across multi-resolutions and explore how the turbulent

mixing plays as a crucial role affecting pollutant concentrations at various resolutions. Furthermore, we seek to determine whether higher-resolution simulations can address the issue of inaccurate turbulent mixing in current models. The Weather Research and Forecasting model coupled with Chemistry (WRF-Chem) is applied to simulate pollutant and meteorological fields during the spring of 2019 in Hefei, a typical mega-city and sub-center of the Yangtze River Delta (YRD) urban agglomeration in China, with a population of nearly 10 million and an area of 11,445 km^2. Our study interprets the various characteristics of black carbon (BC) distributions simulated at multi-resolutions and focuses on the mechanisms involved. BC is selected as the primary pollutant for this study due to its near-inert nature in the atmosphere and can be treated as a representative tracer for turbulent mixing. The paper is organized as follows: Section 2 introduces the WRF-Chem model configuration, the design of multi-resolutions experiments, emissions from different sources, and observational data. Section 3 evaluates model simulations across multi-resolutions against observations, presents the spatial distributions of surface and column concentrations simulated at three resolutions, and investigates the important turbulent mixing processes that generate spatial variability in pollutant concentrations. Section 4 present the conclusion and discussion of the analysis.

2. Methodology

2.1 Models and Experiments

2.1.1 WRF-Chem

The non-hydrostatic Weather Research and Forecasting (WRF) model includes various options for dynamic cores and physical parameterizations that can be used to simulate atmospheric processes over a wide range of spatial and temporal scales (Skamarock et al., 2008). WRF-Chem, the chemistry version of the WRF model (Grell et al., 2005), simulates trace gases and particulates interactively with the meteorological fields. WRF-Chem treats photochemistry of trace gases and aerosol-related processes with various different schemes (e.g. the Statewide Air Pollution Research Center

(SAPRC99) photochemical mechanism and the Model for Simulating Aerosol Interactions and Chemistry (MOSAIC)). In this study, the version of WRF-Chem updated by the University of Science and Technology of China (USTC version of WRF-Chem) is used. Compared with the publicly released version, this USTC version of WRF-Chem includes some additional functions such as the diagnosis of radiative forcing of aerosol species, land surface coupled biogenic VOC (volatile organic compound) emission, aerosol-snow interaction, improved PBL mixing of aerosols and a detailed diagnosis of the contributions of each crucial process to pollutant concentrations (Zhao et al., 2013a; Zhao et al., 2013b; Zhao et al., 2014; Zhao et al., 2016; Hu et al., 2019; Du et al., 2020; Zhang et al., 2021).

The configuration of WRF-Chem in this study is given in Table 1. The SAPRC99 photochemical mechanism (Carter, 2000) is chosen to simulate the gas-phase chemistry, and the MOSAIC is selected for aerosol processes (Zaveri and Peters, 1999; Zaveri et al., 2008). The MOSAIC aerosol scheme includes important physical and chemical processes such as nucleation, condensation, coagulation, aqueous-phase chemistry, and water uptake by aerosols. Sulfate, nitrate, ammonium, sea salt, mineral dust, organic matter (OM), BC, and other (unspecified) inorganics (OIN) constitute the prognostic species in MOSAIC. The aerosol direct effect is coupled to the Rapid Radiative Transfer Model (RRTMG) (Mlawer et al., 1997; Iacono et al., 2000) for both SW (shortwave) and LW (longwave) radiation as implemented by Zhao et al. (2011). We also turned on the aerosol indirect effect, which represents the interactions between aerosols and clouds, including the first and second indirect effects, activation/resuspension, wet scavenging, and aqueous chemistry (Gustafson et al., 2007; Chapman et al., 2009). The photolysis rate is computed by the Fast-J radiation parameterization (Wild et al., 2000). Our simulation includes the secondary organic aerosol (SOA) mechanism, a crucial aerosol process that can substantially reduce discrepancies between simulated results and observations.

Another type of option is meteorological physics, including the Yonsei University (YSU) nonlocal PBL parameterization scheme (Hong et al., 2006), the Noah land-surface model (Chen and Dudhia, 2001) for the surface layer process, the Morrison

two-moment scheme (Morrison et al., 2009) for cloud microphysics, and the Rapid Radiative Transfer Model (RRTMG) for longwave and shortwave radiation. The 25 km resolution simulation turns on the option of cumulus parameterization, which uses the Kain-Fritsch cumulus and shallow convection scheme (Kain, 2004) to simulate sub-grid scale clouds and precipitation. However, this option is turned off in the other two higher resolution simulations because the fine-resolution is sufficient to resolve the cloud forming processes.

2.1.2 Numerical experiments

The study period spans from March 5th to March 20th, 2019. Following previous research (Gustafson et al., 2011), the first five days are considered as the model spin-up time, while the remaining integration period is used for analysis. Consequently, only the results from March 10th to March 20th, 2019, are used in the analysis of this study. Three different resolutions and computational domains are employed in our study. The outer domain, covering East, North, and South China, has 140 x 105 grid cells (107.1°-127.9°E, 17.1°-44.9°N) with a horizontal resolution of 25 km. The middle domain, encompassing the entire YRD region in East China, has 250 x 250 grid cells (111.82°-121.78°E, 27.02°-36.98°N) with a resolution of 5 km. The inner domain, covering most of the Hefei region, consists of 150 x 150 grid cells (116.604°-117.796°E, 31.204°-32.396°N) at a horizontal resolution of 1 km. The center of inner domain is the city of Hefei, a typical mega-city of East China. Hefei, the capital city of Anhui province, is located in the mid-latitude zone with a humid subtropical monsoon climate and serves as a representative case for this study. The regions are shown in Figure S1. To facilitate the comparison of discrepancies among the three simulations at different resolutions, we have selected the innermost region as the main scope of study for this research, as shown in Figure 1a.

In this study, we derive terrain information from a high-resolution (~ 1 km) US Geological Survey (USGS) topographic data and interpolate it onto the WRF grid. Therefore, the three domains with different resolutions exhibit varying degrees of terrain detail. The 1 km grid resolves the most intricate topographic features, followed

235   by the 5 km grid, while the 25 km grid captures the least spatial detail. These multi-

236   resolutions topographic representations potentially influence pollutant turbulent mixing

237   processes, which will be analyzed in this study. The land cover dataset is derived from

238   a 1 km horizontal resolution dataset for China (Zhang et al., 2021). The land use

239   categories follow the United States Geological Survey's (USGS) 24-category

240   classification, and the dataset is based on China's land cover conditions as of 2015. This

241   provides a more accurate representation of current land cover, particularly for eastern

242   China, which has experienced intensive urban expansion since the 2000s. Figure 1b

243   shows the land cover data at different resolutions, with detailed descriptions of the

244   legend and land cover classes provided in Table S1. This set of simulations is referred

245   to as the baseline experiment. With the exception of part of Section 3.2.3, all other

246   analyses in this study are based on the results of these baseline experiments. Moreover,

247   to explore the differences in turbulent mixing simulated at multi-resolutions under

248   consistent land use conditions, we conducted an additional set of sensitivity

249   experiments referred to as the sensitivity experiment. The sensitivity experiment was

250   identical to the baseline experiment, except it used the default USGS land use category

251   data in WRF. Notably, this default USGS data in WRF's geographical static database

252   represents Chinese land use patterns before the 2000s, as shown in Figure S2. This

253   default dataset reflects land use distribution prior to China's significant urbanization.

254   Consequently, the land use data types have minor variations and remained generally

255   consistent across all three resolutions in the sensitivity experiment.

256   On the other hand, the vertical configuration within the PBL is also crucial for

257   accurately modeling pollutant dispersion. To better resolve the PBL structure and

258   mixing processes, we implemented a finer vertical resolution within the PBL. Identical

259   vertical layer distributions are maintained across all three horizontal resolutions (25 km,

260   5 km, and 1 km), ensuring direct comparability of turbulent mixing across different

261   horizontal resolutions. A total of 50 terrain-following vertical eta-layers extending from

262   the surface to approximately 15 km were used in all three resolution simulations, with

263   30 layers distributed below 2 km above the ground to describe the atmospheric

264   boundary structure in detail. The vertical layer was strategically designed with 7 layers

below 200 meters (each approximately 20 meters in height), 3 layers between 200 and 300 meters (each about 30 meters in height), and 8 layers between 300 and 1000 meters (each approximately 80 meters in height). This configuration comprehensively captures mixed layer development and key turbulent processes (e.g., entrainment and surface flux exchange) through layer densification, which is sufficient to capture PBL turbulent mixing. Jiang et al. (2024) and Jiang and Hu (2023) have demonstrated that the number of model vertical layers primarily influences vertical distribution, with more vertical grid layers producing a more stable vertical structure under stable boundary conditions that better resolves boundary layer turbulence.

In order to allow for a straightforward comparison of multi-resolutions simulations and facilitate the identification of differences between the high- and low-resolution simulations, the corner locations of the 1 km and 5 km resolution domains are aligned with the corner locations of the 25 km grid cell. Each grid cell in the 25 km simulation consists of a 5 x 5 set of cells from the 5 km simulation, and each grid cell in the 5 km simulation comprises 5 x 5 cells from the 1 km simulation, as shown in Figure S3. Thus, exactly 25 grids at 5 km resolution and 625 grids at 1 km resolution are embedded within each 25 km grid cell.

To ensure similar boundary forcing across the three simulations, initial and boundary conditions are handled differently for the 25 km, 5 km, and 1 km resolution domains. For the 25 km resolution, meteorological initial and lateral boundary conditions are obtained from the National Center for Environmental Prediction (NCEP) final reanalysis (FNL) data with 1° x 1° resolution and 6 h temporal resolution. Initial and boundary conditions for the trace gases and aerosol species are provided by the quasi-global WRF-Chem simulation with 360 x 145 grid cells (67.5°S-77.5°N, 180°W-180°E) at 1° x 1° resolution. The initial and boundary conditions for the simulation at 5 km resolution are derived from the simulation at 25 km resolution. Similarly, the initial and boundary conditions for the simulation at 1 km resolution are derived from the simulation at 5 km resolution. In this way, since the forcing for the study area is consistent across multi-resolutions, differences in simulation results among multi-resolutions can be attributed to disparities in model resolutions.

295

296 2.1.3 Emissions

297   Anthropogenic emissions for the outer quasi-global simulation are derived from the

298 Hemispheric Transport of Air Pollution version-2 (HTAPv2) at 0.1° x 0.1° horizontal

299 resolution and a monthly temporal resolution for 2010 (Janssens-Maenhout et al., 2015).

300 The Multi-resolution Emission Inventory for China (MEIC) at 0.25° x 0.25° horizontal

301 resolution for 2019 (Li et al., 2017a; Li et al., 2017b) is used to replace emissions over

302 China within the simulation domain. Emission differences significantly contribute to

303 pollutant concentration variability across multi-resolutions. Qian et al. (2010) showed

304 that sub-grid variability of emissions can contribute up to 50% of the variability near

305 Mexico City. To eliminate the impact of inconsistent emissions on pollutant

306 concentrations simulated at multi-resolutions, we ensured emission consistency across

307 all three domains by interpolating emissions for all species from the 25 km resolution

308 domain to both the 5 km and 1 km resolution domains. This study primarily focuses on

309 BC. The spatial distribution of BC emissions is shown in Figure 2. Figure S4 illustrates

310 BC emissions at three different resolutions, demonstrating similar spatial patterns

311 across multi-resolutions. Biomass burning emissions are obtained from the Fire

312 Inventory from NCAR (FINN) at 1 km horizontal resolution and an hour temporal

313 resolution (Wiedinmyer et al., 2011). The diurnal variation of biomass burning

314 emissions follows the suggestions by WRAP (2005), with injection heights based on

315 Dentener et al. (2006) from the Aerosol Comparison between Observations and Models

316 (AeroCom) project. Biogenic emissions were calculated using the Model of Emissions

317 of Gases and Aerosols from Nature (MEGAN) v3.0 model (Guenther, 2007; Zhang et

318 al., 2021).

319

320 **2.2 Observational data**

321 2.2.1 Meteorological data

322   The meteorological data were obtained from the observation tower at the University

323 of Science and Technology of China (USTC) in Hefei, Anhui, China (117.27°E,

324 31.84°N), indicated by a solid black triangle in Figure 1a. The tower measures

temperature, relative humidity, wind speed, and wind direction at 2 m, 4.5 m, 8 m, 12.5 m and 18 m heights. This site represents a typical urban surface within the study area. The tower was installed on the roof of a teaching building, with its top 17 m above the canopy plane. It is equipped with three RM Young 03002 anemometers and three HPM155A temperature and humidity sensors to measure the aforementioned meteorological parameters (Yuan et al., 2016; Liu et al., 2017). This study focuses on analyzing temperature, relative humidity, and wind speed.

Additionally, we employed meteorological data from automatic weather stations (AWSs), which were established based on the operational standards issued by the China Meteorological Administration (CMA, 2018). The hourly data underwent quality control (QC) by local meteorological bureaus of Anhui, following World Meteorological Organization guidelines (Estevez et al., 2011). The QC included checks of consistency, such as internal, temporal-spatial, and climatic range validations. These QC data were used to determine daily mean, minimum, and maximum meteorological variables. The AWSs recorded various parameters, including air temperature (T, °C), wind speed (U, m/s), air pressure (P, Pa), and wind direction. In this study, we focus on the 3-hourly 2 m temperature and 10 m wind speed obtained from four AWS stations located in the study region. The four AWS sites are marked by purple solid dots in Figure S5.

2.2.2 Pollutants data

We used the hourly BC observations from the air quality monitoring site on the campus of USTC during spring (March 10 to March 20, 2019). In this study, we focus on analyzing BC observational data to compare with model output. BC was observed using a Multi-angle Absorption Photometer (MAAP, Model-5012) manufactured by Thermo Scientific. This instrument is located approximately 260 m north of the USTC meteorological tower. It takes advantage of the strong visible light absorption properties of BC aerosols. There is a linear relationship between the attenuation of the beam after passing through the aerosol sample and the load of BC aerosols on the fiber membrane. The BC concentration is derived by inverting this relationship. A light scattering

measurement is incorporated into the chamber to correct for multiple scattering effects caused by particle accumulation on the filter tape. The MAAP-5012 Black Carbon Meter collects atmospheric aerosols using glass fiber filter membranes and observes them at a wavelength of 670 nm.

Although this study primarily focuses on the simulation of BC, we conducted a comprehensive validation of other air pollutants to ensure the reliability of the simulation results. However, after being initially obtained via a parameterized PBL scheme, the mixing coefficients for gases are then clipped to empirically chosen thresholds of 1 m^2/s over rural regions and 2 m^2/s over urban regions, with the distinction between rural and urban regions made based on the local CO emission strength. Thus, the boundary layer mixing coefficient for gases in the WRF-Chem model is implicitly influenced by emission resolution rather than directly controlled by model resolution. Consequently, the existing adjustment process for gas mixing coefficients, which relies on CO emission strength, is unsuitable for studying the impact of model resolution on the turbulent mixing of gaseous pollutants. In contrast, the mixing coefficients for particulate matter are directly calculated through boundary layer parameterization without subsequent modifications. The publicly available version of WRF-Chem defines a default lower limit of 0.1 m²/s for particulate matter mixing coefficients. We did not implement the adjustment proposed by Du et al. (2020), which suggest raising the lower limit of PBL mixing coefficient from 0.1 m^2/s to 5 m^2/s within the PBL. Although setting specific thresholds can improve simulation results, such thresholds are predominantly empirical in nature, whether based on CO and $PM_{2.5}$ emissions or the 5 m²/s threshold suggested by Du et al. (2020). These threshold adjustments effectively compensate for missing physical processes in the model by artificially enhancing mixing intensity. Our approach focuses on understanding the physical mechanisms responsible for the model's underestimation of nighttime mixing intensity, with particular emphasis on how model resolution affects turbulent mixing processes. Rather than employing empirical thresholds to align model output with observations, we aim to investigate the fundamental causes of the discrepancies. We contend that threshold approaches rely heavily on empirical data, lack sufficient

theoretical foundation, and may impede comprehensive understanding of the underlying physical processes. Consequently, this study utilizes the default particulate matter turbulent mixing coefficients in the model for our analyses. In this study, we limited our additional validation to $PM_{2.5}$ (fine particulate matter with aerodynamic diameters less than 2.5 µm), as its mixing processes are governed by the same resolution-dependent mechanisms as BC. Ground observations of hourly $PM_{2.5}$ surface concentrations during March 2019 were obtained from the website of the Ministry of Environmental Protection of China (MEP of China). As our study concentrates on the Hefei region, we selected 10 monitoring stations within this area for detailed analysis. These stations are marked as black triangles in Figure S5.

While hourly observations for both meteorology and pollutants are available, model outputs are provided at 3-hour intervals to balance computational efficiency and storage requirements. Hourly output data would provide higher time resolution but significantly increase storage demands. Given that we ran simulations at multi-resolutions (25 km, 5 km, and 1 km), hourly outputs would have generated prohibitively large data volumes. On the other hand, this 3-hour output interval remains sufficient for our primary research objective of analyzing daily pollutant variations (particularly BC) rather than precise hourly comparisons. This approach effectively captures daily variability patterns without losing essential detail. For direct comparisons, hourly observations were sampled to match our 3-hour model output intervals.

3. Results

3.1 Simulated meteorological fields at various horizontal resolutions

Meteorological fields may play a crucial role in the turbulent mixing and pollutant transport. In this study, we evaluate time series of simulated temperature, wind speed, and relative humidity across three resolutions against observational data to assess resolution impacts on these key meteorological variables. Figure 3a compares the time series of observed and simulated 8-m wind speeds at the USTC site (117.27°E, 31.84°N). Simulation results among multi-resolutions are similar, attributing to

relatively flat and uncomplicated topography. The temporal trends of the simulations closely align with observational data, exhibiting distinct diurnal variations characterized by higher values during the daytime and lower values at night. Additionally, the model struggles to capture some moments accurately, overestimating wind speed when it suddenly increases. For instance, on March 20 at noon, while the observed peak wind speed is approximately 6 m/s, simulations at 25 km and 5 km resolutions produced maximum wind speeds of approximately 9 m/s, significantly exceeding the observed value, with only the 1 km resolution simulation yielding results close to the observation. Figure 3b compares the 2-m temperature simulated at three different resolutions with the observation. The multi-resolutions simulation results exhibit remarkable consistency and closely align with observations. Temperature displays a pronounced diurnal variation, fluctuating between 5 and 30 ℃ with relative stability. However, the model occasionally underestimates or overestimates values at certain time points. As shown in Figure 3c, the multi-resolutions simulated results demonstrate consistency and accurately capture the diurnal variation trend of observed relative humidity (RH). Model results are highly consistent with observations, both reaching a maximum of 100%.

Additionally, Figure S6 displays the time series of observed and simulated meteorological variables averaged across four AWS stations in the study region. Figure S6a presents a comparison of 10-m wind speed simulated at three different resolutions, revealing generally consistent results with observations. The overall pattern is similar to that observed at the single USTC station, characterized by a clear diurnal variation with higher wind speeds during daytime and lower speeds at night. However, simulations at all three resolutions occasionally deviate from observations. For example, on March 11, the 5 km and 1 km resolution models overestimate wind speed at approximately 7 m/s compared to the observed 4 m/s. Conversely, on March 14 during the daytime, all three resolutions underestimate wind speed, simulating around 2 m/s against an observed value of 4 m/s. Figure S6b compares the simulated 2-m temperatures across three resolutions with observational data. The simulated temperatures are remarkably similar across all resolutions and show strong correlation

444 with observations throughout most of the study period. Only a few outliers were noted,

445 which minimally impact the overall pattern. For example, all resolution models

446 overestimate temperature at noon on March 20, simulating approximately 28°C while

447 the observed temperature is only about 20°C.

448 In summary, the simulated meteorological variables across multi-resolutions

449 demonstrate strong similarity and closely match the observations, with only occasional

450 minor discrepancies. However, our subsequent analysis reveals that the variations in

451 pollutant concentrations across multi-resolutions cannot be attributed to the minor

452 discrepancies observed in the time series of meteorological variables.

453

3.2 Simulated BC surface concentrations and impacts of turbulent mixing at various horizontal resolutions

456 3.2.1 Surface concentrations simulated at three different horizontal resolutions

457 The spatial distribution of BC surface concentrations across multi-resolutions in the

458 study area is illustrated in Figure 4. As the resolution improves from 25 km to 5 km and

459 further to 1 km, BC surface concentrations reveal more detailed spatial features. Figure

460 4a presents the simulation results across multi-resolutions, averaged over the whole day.

461 Significant variations exist from coarse resolutions to fine resolutions, with surface

462 concentrations decreasing as resolution increases from 25 km to 5 km and further to 1

463 km. BC surface concentrations range from 0 to 9 ug/m^3. At 25 km resolution, there is a

464 notable discrepancy between the spatial distributions of BC concentrations and

465 emissions (Fig. 2). The highest simulated concentration at 25 km resolution is located

466 west of the USTC site, while maximum emissions are centered at the USTC site. Our

467 analysis indicates that the difference in turbulent mixing between these two regions

468 leads to spatial inconsistency between BC surface concentrations and emissions. The

469 details of this phenomenon will be discussed in section 3.2.2. Figure 4b illustrates the

470 spatial distribution of BC surface concentrations during the daytime. The differences in

471 surface concentrations among multi-resolutions are minimal, with values falling within

472 the range of 0 to 5 ug/m^3. In the central urban areas, the BC surface concentration

473 simulated at 25 km resolution is marginally lower than those simulated at finer

474 resolutions. Moreover, during the daytime, simulated BC concentrations over Chaohu

475 lake areas are notably higher than in other regions, potentially due to the impact of dry

476 deposition velocity. Figure S7 shows the spatial distribution of dry deposition velocity,

477 revealing lower values over lakes compared to other areas. This lower dry deposition

478 velocity leads to higher pollutant concentrations over lakes compared to land areas after

479 pollutants transport to the lake surface during the daytime. At night, dry deposition

480 velocity is similar to that of surrounding non-urban land areas. Consequently, nighttime

481 BC concentrations over lakes are approximately equal to those in surrounding areas.

482 Figure 4c demonstrates the spatial distribution of BC surface concentrations during

483 nighttime. Compared to daytime, BC surface concentrations are notably higher in all

484 major urban regions at night, with high-resolution simulations capturing more spatial

485 variations. In conclusion, BC surface concentrations decrease as resolution increases

486 from 25 km to 5 km and further 1 km. However, the spatial distribution of BC surface

487 concentrations at 5 km and 1 km resolutions are similar throughout the whole day.

488   To facilitate a more accurate and direct comparison of results across multi-

489 resolutions, we refine coarse grids to match fine grids. The detailed refinement process

490 is described in Text S1. Figure S8a exhibits the spatial differences in BC surface

491 concentrations between 25 km and 5 km resolutions, as well as between 25 km and 1

492 km resolutions, averaged over the whole day. It reveals that coarse-resolution (25 km

493 resolution) simulations generally yield higher BC surface concentrations than fine-

494 resolutions (5 km and 1 km resolution) simulations across most areas. The largest

495 disparities mainly occur in central urban areas with complex underlying surfaces and

496 complicated flow patterns. Figure S8b demonstrates the spatial differences in BC

497 surface concentrations between 25 km and 5 km resolutions, as well as between 25 km

498 and 1 km resolutions during the daytime, revealing smaller disparities mostly ranging

499 between -1 and 1 ug/m^3. In contrast, Figure S8c depicts pronounced differences in BC

500 concentrations between 25 km and 5 km resolutions, as well as between 25 km and 1

501 km resolutions during the nighttime, with most areas exhibiting disparities exceeding 2

502 ug/m^3. The largest differences are mainly concentrated in urban areas. These findings

503 indicate that diversities in BC surface concentrations among multi-resolutions are

504   primarily attributable to nocturnal concentrations in urban areas. However, differences

505   between 5 km and 1 km resolutions are small compared to those between 25 km and

506   finer resolutions (5 km and 1 km). BC surface concentrations are approximately equal

507   in the 5 km and 1 km simulations, as shown in Figure S9.

508   Furthermore, BC observations from the USTC monitoring station were utilized to

509   validate the simulated BC surface concentrations. Figure 5 illustrates the diurnal

510   variation of BC surface concentrations averaged over the USTC site. Both observations

511   and simulations exhibit a pronounced diurnal variation, with lower concentrations

512   during the daytime and higher concentrations at night. During the daytime, BC surface

513   concentrations simulated at three resolutions are comparable to the observational data.

514   However, nighttime simulations significantly overestimate BC surface concentrations.

515   As resolution increases from 25 km to 5 km and 1 km, the simulated surface

516   concentrations decrease, aligning more closely with observations. The 25 km resolution

517   simulations yield the highest concentrations, with a maximum value of approximately

518   12 ug/m^3, nearly double the observed values. In contrast, BC surface concentrations

519   simulated at 5 km and 1 km resolutions are similar and more closely align with

520   nocturnal observations, peaking at around 9 ug/m^3. In conclusion, the diurnal variation

521   of the observation is better captured by high-resolution (5 km and 1 km) simulations.

522   The performance of BC surface concentrations across multi-resolutions demonstrates

523   that coarse grid spacing inadequately captures local pollutant distributions.

524   To verify the accuracy and comprehensiveness of the simulation results, we further

525   analyzed the diurnal variation of $PM_{2.5}$ surface concentrations. Figure S10 illustrates

526   the diurnal variation of simulated $PM_{2.5}$ surface concentrations across multi-resolutions

527   compared with observations. The diurnal pattern of $PM_{2.5}$ closely resembles that of BC,

528   characterized by higher concentrations at night and lower concentrations during

529   daytime. Across all resolutions, the model slightly underestimates daytime $PM_{2.5}$

530   surface observations while overestimating nighttime values. Notably, increased

531   horizontal resolution substantially improves nocturnal simulations. The 25 km

532   resolution simulation generates an anomalous midnight peak (105 μg/m³), resulting in

533   a +61% bias, whereas the 5 km and 1 km resolutions substantially mitigate these

534 deviations to approximately 30%. To further examine the contribution of each PM$_{2.5}$

535 component to the diurnal variation across multi-resolutions, Figure S11 shows the

536 diurnal variations of four PM$_{2.5}$ constituents (sulfate (SO$_4^{2-}$), nitrate (NO$_3^-$), OIN, and

537 organic carbon (OC)) averaged over 10 MEP sites in Hefei. Significant differences

538 emerge in the diurnal variations of these components across multi-resolution

539 simulations. Specifically, the surface concentrations of NO$_3^-$, OIN, and OC exhibit a

540 consistent diurnal pattern, with lower concentrations during daytime and higher

541 concentrations at night. As resolution increases from 25 km to 5 km and 1 km, the

542 simulated components surface concentrations decrease, aligning more closely with

543 observations.

544   The total concentration of PM$_{2.5}$ and its components demonstrates significant

545 sensitivity to horizontal resolutions. Coarse resolution simulations underestimate

546 turbulent mixing capacity, resulting in overestimated concentrations. Higher resolution

547 simulations more accurately capture vertical mixing within the PBL. For secondary

548 particles such as sulfates and nitrates, formation rates depend heavily on local precursor

549 substance concentrations (SO$_2$, NO$_x$). Higher resolution simulations may enable more

550 realistic representation of precursor substance diffusion, leading to reduced local

551 concentration gradients and consequently slower secondary aerosol formation rates.

552 Additionally, variations in PM$_{2.5}$ surface concentrations across multi-resolutions may

553 also stem from complex secondary particle generation mechanisms. For instance,

554 liquid-phase oxidation of sulfates in clouds is sensitive to local cloud water distribution,

555 with higher resolutions better capturing small-scale cloud structures that potentially

556 alter sulfate formation efficiency. The formation of ammonium nitrate (NH$_4$NO$_3$) is

557 particularly sensitive to temperature and humidity variations. At higher resolutions,

558 temperature and humidity gradients induced by urban heat island effects or

559 topographical variations can be more realistically simulated, influencing the

560 distribution of gaseous nitric acid (HNO$_3$) and particulate nitrate (NO$_3^-$). Dry deposition

561 processes may also contribute to resolution-dependent variations, as local differences

562 in surface roughness (including buildings and vegetation) become more apparent at

563 higher resolutions, directly affecting particulate deposition velocity rates. Overall, the

564   simulation results for major air pollutants fall within a reasonable error range compared

565   to observational data, confirming the reliability of the model for this study.

566   We now aim to further investigate the underlying factors contributing to the

567   discrepancies in atmospheric pollutant simulations, with a particular focus on BC,

568   across different spatial resolutions. Previous studies have indicated that the diurnal

569   variation of atmospheric particulate matter concentrations is primarily controlled by

570   daily variations of PBL mixing and pollutants emissions (Du et al., 2020). The diurnal

571   variation of BC emissions peak during the daytime and are lower at night. During

572   nighttime, pollutants are trapped within the shallow boundary layer due to the reduced

573   turbulent mixing, resulting in elevated surface concentrations of atmospheric

574   particulate matter. As the boundary layer develops in the morning, pollutants rapidly

575   diffuse and are transported to upper atmospheric layers, leading to relatively low

576   surface concentrations. Therefore, the turbulent mixing process plays a crucial role in

577   determining pollutant concentrations.

578

579   3.2.2 Impacts of turbulent mixing on BC surface concentrations at three different

580   horizontal resolutions

581   To investigate the vertical mixing depth influencing pollutant diffusion, we first

582   analyze the PBL height, as illustrated in Figure 6. Figure 6a shows the spatial

583   distribution of the PBL height simulated at three different resolutions, averaged over

584   the whole day. Higher-resolution simulations yield lower PBL heights and capture more

585   intricate details compared to lower-resolution simulations. This trend is consistent

586   during both daytime and nighttime. Figure 6b demonstrates that the PBL height exceeds

587   0.9 km across most regions during the daytime. Notably, due to strong topographic

588   influences, the PBL height in the vicinity of Chaohu Lake is remarkably low, typically

589   less than 0.1 km. Conversely, in the southwestern region, characterized by higher

590   elevations and more complex terrain, the PBL height surpasses 1.1 km. Figure 6c

591   depicts the nighttime PBL heights at three different resolutions. These heights

592   predominantly fall below 0.3 km, significantly lower than those during the daytime.

593   The PBL height gradually decreases as the resolution increases, which should typically

lead to higher BC surface concentrations. However, BC surface concentrations actually decrease as resolution increases from 25 km to 5 km and 1km (Figure 4). Consequently, the PBL height alone cannot explain the differences in pollutant simulations among multi-resolutions in this study.

Previous studies have established that PBL mixing coefficients are critical determinants in air quality modeling (Du et al., 2020). In WRF-Chem, turbulent mixing within the boundary layer is partially governed by PBL mixing coefficients generated by the PBL parameterization scheme. It is worth noting that the mixing coefficients for atmospheric particulate matter and gases are two distinct variables in the current version of WRF-Chem. The boundary layer mixing coefficient for gases is initially obtained via a parameterized PBL scheme but undergoes additional modification through an empirical parameterization that enhances gas mixing based on CO emission strength (Kuhn et al., 2024). This enhancement applies to gas pollutants when using the MOSAIC aerosol scheme, as implemented in this study. Specifically, gas mixing coefficients are clipped to empirically chosen thresholds of 1 m^2/s over rural regions and 2 m²/s over urban regions, with the distinction between rural and urban regions made based on the local CO emission strength. In contrast, the mixing coefficient of particulate matter is directly calculated through boundary layer parameterization without subsequent modifications. Our study focuses exclusively on the turbulent mixing of atmospheric particulate matter, analyzing the aerosol mixing coefficient with the default lower limit of 0.1 m^2/s as specified in the publicly released version of WRF-Chem. We have not implemented the mixing coefficient adjustments proposed by Du et al. (2020), which suggest raising the lower limit of PBL mixing coefficient from 0.1 m^2/s to 5 m^2/s within the PBL. We contend that threshold approaches are primarily based on empirical data and may impede comprehensive understanding of the underlying physical processes. In our study, particulate matter mixing coefficients are directly calculated through boundary layer parameterization without adjustments based on empirical settings. This approach allows the model to more accurately represent the natural turbulent mixing processes. Consequently, we can investigate the turbulent mixing intensity of particulate matter across different horizontal resolutions and

624   examine the true impact of grid resolution on pollutant mixing.

625   The spatial distribution of aerosol turbulent mixing coefficients at the lowest model

626   layer is analyzed, as shown in Figure 7. Figure 7a illustrates the simulation results

627   across multi-resolutions averaged over the whole day. The variations in PBL mixing

628   coefficients across different resolutions are evident, with high-resolution simulations

629   capturing more spatial characteristics. The spatial distribution of the PBL mixing

630   coefficient demonstrates strong correlation with land use type and terrain height, which

631   will be explored subsequently. Turbulent mixing coefficients range from 0 to 8 m^2/s,

632   with peak values predominantly located in urban areas. Notably, the mixing coefficient

633   simulated at 25 km resolution near surface around USTC substantially exceeds that of

634   the western area, resulting in lower BC surface concentrations simulated at 25 km

635   resolution at USTC compared to its western regions (Figure 4). This discrepancy leads

636   to a mismatch between the spatial distribution of pollutant concentrations and emissions,

637   as discussed in section 3.2.1. During the daytime, the PBL mixing coefficients

638   simulated at three resolutions are relatively high, ranging from 0 to 17 m^2/s, as shown

639   in Figure 7b. BC masses simulated across multi-resolutions are fully mixed within the

640   boundary layer, resulting in similar BC surface concentrations across these resolutions.

641   Conversely, turbulent mixing coefficients diminish considerably during the nighttime,

642   with maximum values approximately 3 m^2/s, as shown in Figure 7c. The turbulent

643   mixing coefficient emerges as one of the important factors controlling surface pollutant

644   concentrations under stable nocturnal PBL conditions. Nighttime PBL coefficients are

645   higher at 5 km and 1 km resolutions compared to 25 km resolution across most of the

646   study area, resulting in lower BC surface concentrations at these two higher resolutions

647   during the nighttime. Figure S12 further illustrates the disparities in parametrized PBL

648   mixing coefficients between 25 km resolution and the two higher-resolution simulations.

649   However, Figure S13 shows that the turbulent mixing coefficient parameterized at 5 km

650   resolution is larger than that at 1 km resolution, which fails to explain the similar surface

651   concentrations in these two higher-resolution (5 km and 1 km) simulations. To further

652   investigate this phenomenon, we selected a meridional section passing through the

653   USTC site to analyze the distribution of vertical wind speed flux, which represents the

22

654　turbulent mixing directly resolved by large-scale dynamic processes.

655　　　Figure 8 displays the cross section of meridional wind speed flux along the USTC

656　site simulated at three different resolutions. The upward vertical wind speed flux

657　simulated at 25 km resolution are near the surface. However, the 5 km resolution

658　simulation generates stronger upward motion at a slightly higher altitude, specifically

659　between 850 and 1000 hPa. Notably, the 1 km resolution simulation captures the highest

660　vertical wind speed flux, with relatively intensive upward motion extending beyond

661　500 hPa. The 1 km resolution can resolve small-scale eddies and capture the most

662　pronounced vertical wind speed fluxes. In comparison, simulations at 5 km resolution

663　are able to capture smaller-scale eddies, while those at 25 km resolution occasionally

664　capture larger-scale eddies. Despite the larger PBL mixing coefficients at 5 km

665　resolution compared to 1 km resolution near the surface, the upward vertical wind speed

666　flux at 1 km resolution reaches higher altitudes, indicating the presence of more small-

667　scale eddies and resulting in enhanced vertical turbulent mixing. Consequently, near the

668　surface, the combined effects of turbulent mixing, which is represented by both the

669　parameterized PBL mixing coefficient and the directly resolved vertical wind speed

670　flux, lead to similar BC surface concentrations at higher resolutions (5 km and 1 km)

671　simulations. Furthermore, Figure S14 shows the meridional cross section during

672　daytime and nighttime. During the day, the mixing height is relatively high at all three

673　resolutions, allowing pollutants to be fully mixed and transported within the PBL. This

674　results in similar BC surface concentrations across multi-resolutions. Conversely, at

675　night, high-resolution simulations resolve more small-scale eddies, resulting in vertical

676　transport reaching higher altitudes and intensifying turbulent mixing. In conclusion,

677　pollutants in lower-resolutions (25 km) simulations tend to accumulate near the surface,

678　whereas at higher resolutions (5 km and 1 km) simulations, pollutants are transported

679　to higher heights. This phenomenon contributes to imparities in BC surface

680　concentration across multi-resolutions.

681

682　3.2.3 Impacts of land use type and terrain height on turbulent mixing coefficients at

683　three different horizontal resolutions

684   Previous analysis indicate that the PBL mixing coefficient is one of the main factors

685   contributing to the disparities in BC surface concentrations across multi-resolutions.

686   Therefore, we further explored the factors influencing the spatial distribution of the

687   PBL mixing coefficient. Our analysis reveals that the spatial distribution of the PBL

688   mixing coefficient is closely related to land use types and terrain height. Specifically,

689   the overall distribution of the turbulent mixing coefficient is closely resembled by the

690   land use types (Figure 1b and Figure 7). However, in areas with obvious magnitude

691   changes, such as east of the USTC site, the turbulent mixing coefficient displays distinct

692   gradient changes that are not reflected in land use patterns. Notably, the spatial

693   distribution of the topographic height (Figure 1a) in this region exhibits distinct gradient

694   changes similar to those of the turbulent mixing coefficients. Consequently, the spatial

695   distribution of the turbulent mixing coefficient is influenced by both terrain and land

696   use types. This correlation can be attributed to the inter-relationship among turbulent

697   mixing, friction velocity, terrain, and land use types. Terrain and land use types

698   influence friction velocity by modifying surface roughness, which in turn directly

699   affects turbulent mixing coefficients within the PBL. Higher surface roughness

700   typically lead to greater fiction velocity, subsequently enhancing turbulent intensity and

701   increasing the vertical mixing efficiency of pollutants within the PBL. To further

702   investigate this relationship, the spatial distribution of friction velocity is analyzed, as

703   shown in Figure 9. The analysis reveals that friction velocity increases as resolution

704   increases from 25 km to 5 km and 1 km resolutions, with finer resolutions (5 km and 1

705   km) capturing more spatial details. Differences in friction velocity are illustrated in

706   Figure S15. The spatial distribution of friction velocity indeed correlates with terrain

707   and land use patterns, consequently influencing the distribution of the PBL mixing

708   coefficient. As a result, the spatial distribution of the PBL mixing coefficient correlates

709   with land use types and terrain height.

710   Our study indicates that variations in land use type distribution simulated at

711   different horizontal resolutions are a significant factor causing changes in PBL mixing

712   coefficients across multi-resolutions. These variations in mixing coefficients relate

713   closely to BC surface concentrations, explaining specific patterns of BC surface

714   concentration distributions. For example, the BC surface concentration south of the

715   USTC site increases as resolution improves from 25 km to 5 km and 1 km resolutions

716   (Figure 4 and Figure S8), contrasting with concentration variations simulated in other

717   regions. Our analysis reveals that the turbulent mixing coefficient simulated at 25 km

718   resolution is higher compared to the two higher-resolution simulations in this area

719   (Figure 7 and Figure S12). Moreover, the spatial distribution of land use types indicates

720   that the 25 km resolution simulation resolves only a single urban land use type in this

721   area (Figure 1b). In contrast, higher resolution simulations capture additional land use

722   types beyond the urban, including lakes, farmland, and shrubs (Figure 1b). The

723   inclusion of these diverse land use types in the higher resolution leads to smaller PBL

724   mixing coefficients in this area, as the surface roughness associated with lakes,

725   farmland, and shrubs is generally lower than that of urban areas. As a result, the reduced

726   vertical mixing in the finer resolution (5 km and 1 km) simulations results in higher BC

727   surface concentrations south of the USTC site.

728   Additionally, to explore the differences in PBL mixing coefficients across multi-

729   resolutions under uniform land use conditions, we designed another set of sensitivity

730   experiments across three resolutions. As mentioned earlier, the only difference from the

731   baseline experiment was the use of the default USGS land use classification data in the

732   WRF model. As shown in Figure S2, land use type data at different horizontal

733   resolutions are approximately consistent in this setup. All other settings remained

734   identical to those in the baseline experiment.

735   Figure 10 presents the spatial distribution of PBL mixing coefficients in the

736   sensitivity experiment. Figure 10a illustrates the results across multi-resolutions

737   averaged over the whole day. Similar to the baseline experiment, increasing resolution

738   resolves more spatial details. For example, in the area where the USTC site is located,

739   the PBL mixing coefficient in the 25 km resolution simulation of the sensitivity

740   experiment is approximately 4.3 m²/s, significantly lower than the 8 m²/s observed in

741   the baseline experiment. This pattern is consistent across higher resolutions (5 km and

742   1 km). This finding aligns with the spatial distribution of land use types used in both

743   sets of experiments (Figure 1b and Figure S2). The decrease in mixing coefficients in

744   the sensitivity experiment stems from its land use data failing to resolve urban land

745   types in urban areas. Figures 10b and 10c show the PBL mixing coefficients of the

746   sensitivity experiment during daytime and nighttime, respectively. Consistent with the

747   baseline experiment, the turbulent mixing coefficients during the day are substantially

748   higher than at night. The PBL coefficients in the nighttime simulations are higher at 5

749   km and 1 km resolutions compared to the 25 km resolution.

750   Additionally, Figure S16 further illustrates the differences in the parameterized

751   PBL mixing coefficient between the 25 km resolution and the two higher-resolution

752   simulations under roughly uniform land use conditions. Figure S16c shows that in the

753   city center, the boundary layer mixing coefficient parameterized at 5 km and 1 km

754   resolutions is higher than at the 25 km resolution during nighttime. Since urban areas

755   are primarily flat, topographical differences between different resolutions in urban areas

756   are minimal, almost negligible. Furthermore, because the land use types in the

757   sensitivity experiment are approximately consistent across different resolutions, the

758   main factor responsible for resolution-related differences in the PBL mixing

759   coefficients in urban areas is the grid size. Notably, in areas with significant topographic

760   variations, such as suburban and rural regions, the difference in boundary layer mixing

761   coefficients between 25 km and 5 km/1 km resolutions in the sensitivity experiment

762   strongly correlates with the spatial distribution of topographic differences. This directly

763   demonstrates that topographic height is also a key determinant of boundary layer

764   mixing coefficient distribution. Qian et al. (2010) indicated that the terrain affects the

765   transport and mixing of aerosols and trace gases, as well as their concentrations across

766   multi-resolutions, through its impact on meteorological fields such as wind and the PBL

767   structure. These terrain-related effects are particularly significant in regions with more

768   variable topography. Additionally, Figure S17 shows that the turbulent mixing intensity

769   parameterized at 5 km resolution in the sensitivity experiment is greater than at 1 km

770   resolution. Further analysis of the latitude-pressure cross section of BC concentrations

771   and vertical wind speed flux, as shown in Figure S18, indicates that, similar to the

772   baseline experiment, the 1 km resolution of the sensitivity experiment resolves more

773   small-scale turbulent eddies, capturing more prominent vertical wind speed flux, thus

774   resulting in stronger turbulent mixing.

775   Through comprehensive analysis of both baseline and sensitivity experiments, we

776   found that within the resolution range of 25 km to 5 km and 1 km, the spatial distribution

777   accuracy of land use types plays a decisive role in parameterizing the PBL mixing

778   coefficient. Finer land use type information at higher resolutions directly alters the

779   spatial distribution of the boundary layer mixing coefficient, with urban surfaces

780   significantly increasing the parameterized PBL mixing coefficient. Therefore,

781   accurately representing land use types, particularly urban surfaces, is critical for

782   parameterizing the PBL mixing coefficient. On the other hand, in the sensitivity

783   experiment, complex terrain areas with significant elevation (such as suburban, rural,

784   and hilly regions) increase mixing coefficients by enhancing surface roughness,

785   whereas this effect is weaker in flat urban areas. Consequently, differences in PBL

786   mixing coefficients across multi-resolutions strongly correlate with terrain precision.

787   Higher resolutions can resolve finer terrain variations, affecting local turbulent mixing

788   (such as terrain-induced mechanical turbulence). This confirms the dominant role of

789   high-resolution terrain and land use information in PBL mixing coefficient

790   parameterization. Notably, in regions where land use types and terrain height remain

791   relatively flat and consistent across different horizontal resolutions in the sensitivity

792   experiments, increasing resolution still leads to enhanced boundary layer mixing

793   coefficients, highlighting the importance of grid size for parameterizing the boundary

794   layer mixing coefficient. In the resolution range from 5 km to 1 km, higher resolution

795   slightly reduces the parameterized boundary layer mixing coefficient. However, the 1

796   km resolution model resolves more small-scale turbulent eddies, resulting in stronger

797   turbulent mixing at night. In summary, for parameterization of boundary layer mixing

798   coefficients across multi-resolutions, high-resolution surface information is more

799   important in regions with significant changes in land use types and terrain height. Grid

800   size is also crucial in regions with more gradual changes, where higher-resolution grids

801   consistently enhance boundary layer mixing representation. Therefore, to improve PBL

802   mixing coefficient simulation, priority should be given to ensuring accuracy of land use

803   data (especially spatial representation of urban types), precise terrain representation in

804　complex regions, and appropriated grid resolution to enhance turbulent mixing

805　simulation.

806

807　3.3 Simulated BC column concentrations and impacts of turbulent mixing at

808　various horizontal resolutions

809　3.3.1 Simulated BC column concentrations at three different horizontal resolutions

810　　It is generally accepted that the turbulent mixing process primarily affects

811　pollutant surface concentrations by mixing surface pollutants into higher layers,

812　without altering the column concentration. However, in this study, BC column

813　concentrations exhibit differences across multi-resolutions simulations. Therefore, we

814　further investigate the spatial distribution of BC column concentrations and the main

815　mechanisms behind these variations. Figure 11a illustrates the spatial distribution of

816　BC column concentrations simulated at three resolutions, averaged over the whole day.

817　The regional average values for the three resolutions are 2041, 2150, and 2223 ug/m^2,

818　respectively. The 5 km and 1 km resolution simulations yield larger BC column

819　concentrations compared to 25 km resolution simulations. The spatial distribution of

820　BC column concentrations simulated at 25 km resolution is highly consistent with the

821　BC emission distributions (Figure 2), showing high concentrations in central urban

822　areas exceeding 2500 ug/m^2, while regions distant from urban centers demonstrate

823　lower concentrations, generally below 2100 ug/m^2. The 5 km resolution simulation

824　results indicate peak column concentrations concentrated in urban areas and spread

825　around, with the southwestern area approaching 2250 ug/m^2. The 1 km resolution

826　simulation results yield the largest BC column concentrations and demonstrate the most

827　pronounced diffusion tendency, with most areas exceeding 2250 ug/m^2. Figure 11b and

828　Figure 11c reveal lower BC column concentrations during the daytime compared to

829　those at night, with a more pronounced dispersion trend of column concentrations

830　simulated at night. Figure S19 depicts the differences in BC column concentrations

831　between 25 km and 5 km resolutions, as well as between 25 km and 1 km resolutions,

832　revealing that BC column concentrations in coarser resolutions are marginally lower

833　than those in finer resolutions (5 km and 1 km) in most of the study areas. On the other

834   hand, the BC column concentration simulated at 1 km resolution are larger than those

835   at 5 km resolution, as shown in Figure S20. In conclusion, BC column concentrations

836   increases with increased resolutions, accompanied by a more pronounced dispersion

837   tendency towards higher and farther areas.

838

839   3.3.2 Impacts of turbulent mixing on BC column concentrations at three different

840   horizontal resolutions

841   We further analyze the mechanisms underlying the differences in BC column

842   concentrations across multi-resolutions in urban areas. Figure 12a displays the vertical

843   profiles of BC concentrations averaged over the study area. The BC profiles at 25 km

844   resolution exhibit significant variability, generally decreasing from the surface to higher

845   altitudes. The near-surface BC concentration is approximately three times higher than

846   those at high altitudes, with surface concentrations reaching about 3 ug/m^3. At an

847   altitude of 100 m, the concentration drops to 1 ug/m^3, while above this elevation, the

848   BC concentration is less than 1 ug/m^3. Substantial disparities exist among multi-

849   resolutions simulations in the vertical profiles of BC concentrations. Our analyses

850   above have shown that near the surface, the parameterized mixing coefficients and

851   directly resolved vertical wind speed flux are lower at 25 km resolution compared to 5

852   km and 1 km resolutions, reducing the vertical mixing of pollutants in 25 km resolution

853   simulations. Thus, BC concentrations at 25 km resolution are higher near the surface

854   and lower at higher altitudes compared to high-resolution (5 km and 1 km) simulations.

855   Moreover, the parametrized PBL mixing coefficient at 1 km resolution is lower than at

856   5 km resolution in the atmosphere, but the directly resolved upward vertical wind speed

857   flux by the model dynamic process reaches higher altitudes at 1 km resolution compared

858   to 5 km resolution. Thus, due to the combined effects of these two processes, the

859   intensity of turbulent mixing is similar between the 5 km and 1 km resolutions at near-

860   surface levels, whereas it is greater at 1 km resolution than at 5 km resolution at higher

861   altitudes. In numerical models, sub-grid scale (SGS) turbulent diffusion is typically

862   simulated by parameterization schemes. However, as model resolution increases, such

863   as achieving 1 km resolution, the turbulent mixing is increasingly resolved by

864   dynamical framework of the model. This advancement allows the model to capture

865   dynamic structures and small-scale turbulence more accurately, significantly enhancing

866   the strength of turbulent mixing. The resolution of dynamic processes reduces reliance

867   on traditional parameterization schemes, thereby decreasing the PBL mixing coefficient

868   parameterized at finer resolutions. In conclusion, at higher altitudes, the enhanced

869   turbulent mixing efficiently facilitates more ground-emitted pollutants to higher height

870   as resolution increases. Thus, BC concentrations at 5 km and 1 km resolution are similar

871   near surface, with 1 km resolution yielding the largest concentrations at higher altitudes.

872   To further investigate the BC column concentrations and their dispersion tendency

873   towards farther areas, we analyzed the vertical profile of wind speed at three resolutions

874   averaged over the study area, as shown in Figure 12b. The vertical profile of wind speed

875   is relatively consistent across the three resolutions. From the ground to higher altitudes,

876   the overall wind speed gradually increases, transitioning from low speeds near the

877   surface to higher speeds aloft. Near the ground, the simulated average wind speed is

878   approximately 1 m/s, increasing to 4 m/s at an altitude of 1 km, and reaching an average

879   of about 7 m/s at an altitude of 2 km. In the upper atmosphere, characterized by larger

880   wind speeds, pollutants mixed up from near-surface can be transported and dispersed

881   farther. As previously mentioned, BC simulated in higher-resolution simulations can be

882   transported to higher altitudes, thus dispersing over greater distances by stronger winds.

883   Therefore, as the resolution increases, the trend of diffusion towards farther regions in

884   the simulated BC column concentrations becomes more pronounced.

885   As previously discussed, higher-resolution simulations facilitate BC transport to

886   greater altitudes and further distances. This phenomenon extends its atmospheric

887   lifetime, consequently resulting in increased column concentrations. Bauer et al. (2013)

888   noted that turbulent mixing and convective transport processes play a critical role in

889   determining BC lifetimes. Figure 13 illustrates the spatial distribution of BC lifetime,

890   calculated by dividing the BC column concentration by the dry deposition flux. It

891   demonstrates that BC lifetime gradually lengthens as resolution increases. The average

892   lifetime of BC column concentrations in the study area is 344 h, 350 h, and 382 h for

893   25 km, 5 km, and 1 km resolutions, respectively. These results clearly demonstrate that

894 BC simulated at higher resolutions exhibits prolonged atmospheric residence times.

895 Consequently, the BC column concentration is higher in high-resolution simulations.

896

4. Conclusion and Discussion

898   Turbulent mixing plays a crucial role in urban pollutant transport by enhancing the

899 diffusion of atmospheric pollutants. Current atmospheric models often underestimate

900 turbulent exchange within stable nocturnal boundary layers, and the turbulent mixing

901 varies markedly across different model horizontal resolutions. However, few studies

902 have analyzed how turbulent mixing processes across multi-resolutions affect pollutant

903 concentrations in urban areas. Therefore, our goal is to elucidate the variations in

904 pollutant concentrations across multi-resolutions and investigate the influence of

905 turbulent mixing on pollutant concentrations at various resolutions.

906   We conducted a three-nested WRF-Chem simulation at 25 km, 5 km, and 1 km

907 resolutions in the Hefei area. BC surface concentrations decrease as resolution increases

908 from 25 km to 5 km and further to 1 km but are similar at 5 km and 1 km resolutions,

909 showing significant diurnal variations with higher concentrations at night and lower

910 during the daytime. The BC surface concentrations across multi-resolutions align well

911 with USTC site observations during daytime but are overestimated at night, with this

912 overestimation decreasing at higher-resolution (5 km and 1 km). Disparities in BC

913 surface concentrations between the two finer-resolution and the 25 km resolution

914 simulations are primarily attributable to nocturnal concentrations. In addition, the

915 diurnal variation of $PM_{2.5}$ surface concentrations simulated at different resolutions

916 follows the same trend as the observed concentrations at the national monitoring sites,

917 with slight underestimation during daytime and overestimation at night. The PBL

918 mixing coefficient plays a crucial role in controlling surface particulate matter

919 concentrations at night. Larger nighttime PBL mixing coefficients and higher vertical

920 wind speed flux at 5 km and 1 km resolutions compared to 25 km resolution near the

921 surface result in lower BC surface concentrations. However, the PBL mixing coefficient

922 at 5 km is larger than at 1 km resolution. Moreover, the upward vertical wind speed flux

resolved at 1 km resolution reaches higher altitudes compared to 25 km and 5 km resolutions, indicating more small-scale eddies and resulting in enhanced turbulent mixing. Consequently, near the surface, the combined effects of parametrized PBL mixing coefficient and the directly resolved vertical wind speed flux lead to similar BC surface concentrations at 5 km and 1 km resolutions.

Further analysis reveals that the spatial distribution of PBL mixing coefficients is influenced by both land use types and terrain heights. The turbulent mixing coefficient correlates with the spatial distribution of land use types at smaller scales, with urban underlying surfaces notably increasing the parameterized PBL mixing coefficient. The mixing coefficient also strongly correlates with terrain heights at larger scales, particularly in regions with complex topography and significant elevation differences, where higher terrain substantially enhances mixing coefficients. This correlation can be attributed to the interrelationship among turbulent mixing coefficients, friction velocity, terrain, and land use types. The static database of terrain and land use types employed as model input determines the surface roughness. Higher surface roughness typically leads to greater fiction velocity, subsequently increasing the PBL mixing coefficients. Moreover, in regions where land use types and terrain height remain relatively flat and consistent across multi-resolutions, increasing resolution still enhances boundary layer mixing coefficients, highlighting the importance of grid size. Thus, both surface information and grid resolution are crucial for accurately parameterizing PBL mixing coefficients, with priority given to accurate land use data, precise terrain representation, and higher grid resolution to improve turbulent mixing simulations.

In WRF-Chem, the mixing coefficients of chemical species are clipped to empirically chosen thresholds of 1 m^2/s over rural areas and 2 m^2/s over urban areas to prevent unrealistically low values. These thresholds are modified based on differences in anthropogenic CO and primary $PM_{2.5}$ emissions between rural and urban regions. Importantly, this adjustment applies exclusively to gases and not to aerosols when the MOSAIC or MADE/SORGAM aerosol schemes are used. This is because the adjustment does not couple with the aerosol PBL mixing scheme in WRF-Chem, although potential modifications could be made for compatibility with the MOSAIC or

MADE/SORGAM scheme. Thus, the boundary layer mixing coefficient for gases is implicitly influenced by emission resolution rather than directly controlled by model resolution. In this study, this treatment caused gas mixing coefficients to converge across different horizontal resolutions, preventing us from accurately assessing the impact of horizontal resolution on gas turbulent mixing. For aerosols, however, the original PBL mixing coefficients are retained, which are directly parametrized from boundary layer parameterization schemes. Therefore, our focus is mainly on particulate matter in this analysis and we omitted this modification for gases.

The variations in turbulent mixing across multi-resolution simulations not only affect the BC surface concentration but also lead to different BC column concentrations. BC column concentrations increase with improved resolutions, accompanied by a more pronounced diffusion tendency towards higher altitudes and distant regions. Throughout the atmosphere, turbulent mixing intensifies with improved resolutions, resulting in pollutants being transported to higher altitudes. Concurrently, wind speed increases with altitude, facilitating the pollutants which are mixed to higher altitudes to be spread farther. Consequently, BC simulated at higher resolution is transported to greater altitudes and dispersed to farther regions, thus persisting in the atmosphere for longer periods and leading to larger lifetimes. As a result, BC column concentrations increase with finer resolutions.

This study highlights the importance of model horizontal resolution in simulating the dispersion of atmospheric pollutants. We observed that the enhanced turbulent mixing strength in high-resolution can more accurately reproduce the vertical and horizontal distribution of pollutants, thus aligning the simulated pollutant surface concentrations more closely with actual observations. In contrast, turbulent mixing in low-resolution simulations, primarily depending on boundary layer parameterizations, may not adequately capture the dynamics of turbulence, leading to discrepancies between the simulated and actual distribution of pollutants, particularly during the night with stable boundary condition. Future research should focus on improving PBL parameterization schemes to enhance model performance at lower resolutions, thereby better serving the needs of air pollution control and environmental management.

983   We have noted that the parameterized PBL mixing coefficient decreases when

984   transitioning from 5 km to 1 km resolution, alongside an increase in vertical wind speed

985   flux which represents turbulent mixing directly resolved by the dynamical processes.

986   This trend suggests that if the resolution was further increased to LES scales, the

987   parameterized PBL mixing coefficient might diminish significantly, potentially

988   approaching zero, while the turbulence mixing resolved directly by the dynamics would

989   intensify considerably. At LES scales, the majority of turbulent mixing is directly

990   resolved, capturing the atmospheric dynamical processes and turbulent exchanges more

991   realistically, thereby reducing the simulation biases caused by parameterization errors.

992   This shift diminishes reliance on traditional boundary layer parameterizations to

993   simulate turbulent mixing, leading to a substantial reduction in the parameterized

994   boundary layer mixing coefficient. By capturing the finer details of atmospheric

995   dynamics, the model provides a more realistic representation of turbulent mixing and

996   related physical processes, which is crucial for understanding weather patterns, climate

997   variability, and pollutant dispersion. However, due to the huge computational resources

998   required for LES simulation, we have not yet performed an analysis at the LES scale,

999   but it is worth further exploring in the future.

1000   Moreover, in addition to the influence of surface roughness on turbulence intensity,

1001   surface type significantly affects the CBL and turbulence mixing strength through

1002   differences in radiative flux absorption, reflection, and heat exchange. There are

1003   substantial variations in the absorption and reflection of shortwave radiation across

1004   different surface types. Urban areas typically have lower albedo, absorbing more

1005   shortwave radiation, which increases surface temperature and transfers energy to the

1006   atmosphere as sensible heat. In contrast, vegetated areas generally have higher albedo

1007   and, through transpiration, release more latent heat while reducing sensible heat output.

1008   These differences in energy exchange between surface and atmosphere directly

1009   influence turbulence strength. Furthermore, the varying balance between sensible and

1010   latent heat fluxes across different surface types impacts turbulence intensity and CBL

1011   depth. For instance, urban areas, with stronger sensible heat flux, tend to generate more

1012   intense thermal convection, often resulting in a shallower CBL, while vegetated areas,

with predominant latent heat flux, may develop more stable atmospheric conditions, potentially leading to a deeper CBL with weaker turbulence. These mechanisms of radiative absorption and heat exchange are crucial in the formation of the diurnal CBL and determining turbulence intensity. Future studies on land use impacts on turbulence mixing should therefore consider not only surface roughness but also radiative flux differences, sensible and latent heat exchange mechanisms, and the comprehensive effects of surface albedo on turbulence development.

Our analysis also found that higher-resolution facilitate transport over greater distances, suggesting that inter-city pollutant diffusion can be affected by model resolution, with coarse-resolution potentially reducing long-range transport and inter-urban impacts. While previous studies have examined pollutant formation mechanisms at specific resolutions and explored the physical and chemical interactions among megacities, few have considered the impacts of different resolutions on long-range transport between cities. Due to computational cost constraints, inter-urban impacts are not discussed in this study but deserve further investigation in the future. Finally, while vertical resolution is held constant in our study, we recognize that it could influence the interpretation of the turbulence processes in certain scenarios, especially in regions with complex vertical structures. Therefore, future work could systematically explore the interplay between vertical resolution and pollutant concentration or aerosol-boundary layer feedbacks.

Author contributions. ZY and CZ designed the experiments and conducted and analyzed the simulations. All authors contributed to the discussion and final version of the paper.

Competing interests. The contact author has declared that none of the authors has any competing interests.

Reference

Banks, R. F. and Baldasano, J. M.: Impact of WRF model PBL schemes on air quality simulations over Catalonia, Spain, Science of the Total Environment, 572, 98-113, https://doi.org/10.1016/j.scitotenv.2016.07.167, 2016.

Bauer, S. E., Bausch, A., Nazarenko, L., Tsigaridis, K., Xu, B., Edwards, R., Bisiaux, M., and McConnell, J.: Historical and future black carbon deposition on the three ice caps: Ice core measurements and model simulations from 1850 to 2100, Journal of Geophysical Research-Atmospheres, 118, 7948-7961, https://doi.org/10.1002/jgrd.50612, 2013.

Berger, A., Barbet, C., Leriche, M., Deguillaume, L., Mari, C., Chaumerliac, N., Begue, N., Tulet, P., Gazen, D., and Escobar, J.: Evaluation of Meso-NH and WRF-CHEM simulated gas and aerosol chemistry over Europe based on hourly observations, Atmospheric Research, 176, 43-63, https://doi.org/10.1016/j.atmosres.2016.02.006, 2016.

Carter: Implementation of the SAPRC-99 chemical mechanism into the models-3 framework, 2000.

Chan, C. K. and Yao, X.: Air pollution in mega cities in China, Atmospheric Environment, 42, 1-42, https://doi.org/10.1016/j.atmosenv.2007.09.003, 2008.

Chapman, E. G., Gustafson, W. I., Jr., Easter, R. C., Barnard, J. C., Ghan, S. J., Pekour, M. S., and Fast, J. D.: Coupling aerosol-cloud-radiative processes in the WRF-Chem model: Investigating the radiative impact of elevated point sources, Atmospheric Chemistry and Physics, 9, 945-964, https://doi.org/10.5194/acp-9-945-2009, 2009.

Chen, F. and Dudhia, J.: Coupling an Advanced Land Surface–Hydrology Model with the Penn State–NCAR MM5 Modeling System. Part I: Model Implementation and Sensitivity, Monthly Weather Review, 129, 569-585, 2001.

Chen, Y., Zhao, C., Zhang, Q., Deng, Z., Huang, M., and Ma, X.: Aircraft study of Mountain Chimney Effect of Beijing, China, Journal of Geophysical Research-Atmospheres, 114, https://doi.org/10.1029/2008jd010610, 2009.

CMA, 2018: Technical Specifications for Maintenance of Regional Automatic Weather Stations. QX/T 465–2018. (in Chinese). Available at: http://cmastd.cmatc.cn/standardView.jspx?id=3076. Accessed on 5 May 2022., 2018.

Costa, F. D., Acevedo, O. C., Mombach, J. C. M., and Degrazia, G. A.: A Simplified Model for Intermittent Turbulence in the Nocturnal Boundary Layer, Journal of the Atmospheric Sciences, 68, 1714-1729, https://doi.org/10.1175/2011jas3655.1, 2011.

Cuchiara, G. C., Li, X., Carvalho, J., and Rappenglueck, B.: Intercomparison of planetary boundary layer parameterization and its impacts on surface ozone concentration in the WRF-Chem model for a case study in Houston/Texas, Atmospheric Environment, 96, 175-185, https://doi.org/10.1016/j.atmosenv.2014.07.013, 2014.

Dentener, F., Kinne, S., Bond, T., Boucher, O., Cofala, J., Generoso, S., Ginoux, P., Gong, S., Hoelzemann, J. J., Ito, A., Marelli, L., Penner, J. E., Putaud, J. P., Textor, C., Schulz, M., van der Werf, G. R., and Wilson, J.: Emissions of primary aerosol and precursor gases in the years 2000 and 1750 prescribed data-sets for AeroCom, Atmospheric Chemistry and Physics, 6, 4321-4344, https://doi.org/10.5194/acp-6-4321-2006, 2006.

Du, Q., Zhao, C., Zhang, M., Dong, X., Chen, Y., Liu, Z., Hu, Z., Zhang, Q., Li, Y., Yuan, R., and Miao, S.: Modeling diurnal variation of surface $PM_{2.5}$ concentrations over East China with WRF-Chem: impacts from boundary-layer mixing and anthropogenic emission, Atmospheric Chemistry and Physics, 20, 2839-2863, https://doi.org/10.5194/acp-20-2839-2020, 2020.

Estevez, J., Gavilan, P., and Giraldez, J. V.: Guidelines on validation procedures for meteorological data from automatic weather stations, Journal of Hydrology, 402, 144-154, https://doi.org/10.1016/j.jhydrol.2011.02.031, 2011.

Fountoukis, C., Koraj, D., van der Gon, H. A. C. D., Charalampidis, P. E., Pilinis, C., and Pandis, S. N.: Impact of grid resolution on the predicted fine PM by a regional 3-D chemical transport model, Atmospheric Environment, 68, 24-32,

https://doi.org/10.1016/j.atmosenv.2012.11.008, 2013.

Grell, G. A., Peckham, S. E., Schmitz, R., McKeen, S. A., Frost, G., Skamarock, W. C., and Eder, B.: Fully coupled "online" chemistry within the WRF model, Atmospheric Environment, 39, 6957-6975, https://doi.org/10.1016/j.atmosenv.2005.04.027, 2005.

Guenther, A.: Estimates of global terrestrial isoprene emissions using MEGAN (Model of Emissions of Gases and Aerosols from Nature) (vol 6, pg 3181, 2006), Atmospheric Chemistry and Physics, 7, 4327-4327, https://doi.org/10.5194/acp-7-4327-2007, 2007.

Gustafson, W. I., Jr., Qian, Y., and Fast, J. D.: Downscaling aerosols and the impact of neglected subgrid processes on direct aerosol radiative forcing for a representative global climate model grid spacing, Journal of Geophysical Research-Atmospheres, 116, https://doi.org/10.1029/2010jd015480, 2011.

Gustafson, W. I., Jr., Chapman, E. G., Ghan, S. J., Easter, R. C., and Fast, J. D.: Impact on modeled cloud characteristics due to simplified treatment of uniform cloud condensation nuclei during NEAQS 2004, Geophysical Research Letters, 34, https://doi.org/10.1029/2007gl030021, 2007.

Han, S., Bian, H., Tie, X., Xie, Y., Sun, M., and Liu, A.: Impact of nocturnal planetary boundary layer on urban air pollutants: Measurements from a 250-m tower over Tianjin, China, Journal of Hazardous Materials, 162, 264-269, https://doi.org/10.1016/j.jhazmat.2008.05.056, 2009.

Holmes, H. A., Sriramasamudram, J. K., Pardyjak, E. R., and Whiteman, C. D.: Turbulent Fluxes and Pollutant Mixing during Wintertime Air Pollution Episodes in Complex Terrain, Environmental Science & Technology, 49, 13206-13214, https://doi.org/10.1021/acs.est.5b02616, 2015.

Hong, S.-Y., Noh, Y., and Dudhia, J.: A new vertical diffusion package with an explicit treatment of entrainment processes, Monthly Weather Review, 134, 2318-2341, https://doi.org/10.1175/mwr3199.1, 2006.

Hu, Z., Huang, J., Zhao, C., Bi, J., Jin, Q., Qian, Y., Leung, L. R., Feng, T., Chen, S., and Ma, J.: Modeling the contributions of Northern Hemisphere dust sources to

dust outflow from East Asia, Atmospheric Environment, 202, 234-243, https://doi.org/10.1016/j.atmosenv.2019.01.022, 2019.

Iacono, M. J., Mlawer, E. J., Clough, S. A., and Morcrette, J. J.: Impact of an improved longwave radiation model, RRTM, on the energy budget and thermodynamic properties of the NCAR community climate model, CCM3, Journal of Geophysical Research-Atmospheres, 105, 14873-14890, https://doi.org/10.1029/2000jd900091, 2000.

Janssens-Maenhout, G., Crippa, M., Guizzardi, D., Dentener, F., Muntean, M., Pouliot, G., Keating, T., Zhang, Q., Kurokawa, J., Wankmueller, R., van der Gon, H. D., Kuenen, J. J. P., Klimont, Z., Frost, G., Darras, S., Koffi, B., and Li, M.: HTAP_v2.2: a mosaic of regional and global emission grid maps for 2008 and 2010 to study hemispheric transport of air pollution, Atmospheric Chemistry and Physics, 15, 11411-11432, https://doi.org/10.5194/acp-15-11411-2015, 2015.

Jia, W. and Zhang, X.: Impact of modified turbulent diffusion of $PM_{2.5}$ aerosol in WRF-Chem simulations in eastern China, Atmospheric Chemistry and Physics, 21, 16827-16841, https://doi.org/10.5194/acp-21-16827-2021, 2021.

Jia, W., Zhang, X., Zhang, H., and Ren, Y.: Application of Turbulent Diffusion Term of Aerosols in Mesoscale Model, Geophysical Research Letters, 48, https://doi.org/10.1029/2021gl093199, 2021.

Jiang, L. and Hu, J.: Influence of the lowest model level height and vertical grid resolution on mesoscale meteorological modeling, Atmospheric Research, 296, https://doi.org/10.1016/j.atmosres.2023.107066, 2023.

Jiang, L., Bessagnet, B., Meleux, F., Couvidat, F., Tognet, F., and Hu, J.: The role of vertical grid resolution and turbulent diffusion uncertainty on chemical transport modeling, Atmospheric Research, 312, https://doi.org/10.1016/j.atmosres.2024.107759, 2024.

Kain, J. S.: The Kain-Fritsch convective parameterization: An update, Journal of Applied Meteorology, 43, 170-181, https://doi.org/10.1175/1520-0450(2004)043<0170:Tkcpau>2.0.Co;2, 2004.

Kim, S. W.: The Influence of PBL Parameterizations on the Distributions of Chemical

Species in a Mesoscale Chemical Transport Model, WRF-Chem,

Kuhn, L., Beirle, S., Kumar, V., Osipov, S., Pozzer, A., Boesch, T., Kumar, R., and Wagner, T.: On the influence of vertical mixing, boundary layer schemes, and temporal emission profiles on tropospheric NO2 in WRF-Chem - comparisons to in situ, satellite, and MAX-DOAS observations, Atmospheric Chemistry and Physics, 24, 185-217, https://doi.org/10.5194/acp-24-185-2024, 2024.

Li, H., Li, L., Huang, C., An, J., Yan, R., Huang, H., Wang, Y., Lu, Q., Wang, Q., Lou, S., Wang, H., Zhou, M., Tao, S., Qiao, L., and Chen, M.: Ozone Source Apportionment at Urban Area during a Typical Photochemical Pollution Episode in the Summer of 2013 in the Yangtze River Delta, Environmental Science, 36, 1-10, 2015.

Li, L., An, J., Huang, L., Yan, R., Huang, C., and Yarwood, G.: Ozone source apportionment over the Yangtze River Delta region, China: Investigation of regional transport, sectoral contributions and seasonal differences, Atmospheric Environment, 202, 269-280, https://doi.org/10.1016/j.atmosenv.2019.01.028, 2019.

Li, M., Liu, H., Geng, G., Hong, C., Liu, F., Song, Y., Tong, D., Zheng, B., Cui, H., Man, H., Zhang, Q., and He, K.: Anthropogenic emission inventories in China: a review, National Science Review, 4, 834-866, https://doi.org/10.1093/nsr/nwx150, 2017a.

Li, M., Zhang, Q., Kurokawa, J.-i., Woo, J.-H., He, K., Lu, Z., Ohara, T., Song, Y., Streets, D. G., Carmichael, G. R., Cheng, Y., Hong, C., Huo, H., Jiang, X., Kang, S., Liu, F., Su, H., and Zheng, B.: MIX: a mosaic Asian anthropogenic emission inventory under the international collaboration framework of the MICS-Asia and HTAP, Atmospheric Chemistry and Physics, 17, 935-963, https://doi.org/10.5194/acp-17-935-2017, 2017b.

Li, Q., Zhang, H., Jin, X., Cai, X., and Song, Y.: Mechanism of haze pollution in summer and its difference with winter in the North China Plain, Science of the Total Environment, 806, https://doi.org/10.1016/j.scitotenv.2021.150625, 2022.

Li, Q., Wu, B., Liu, J., Zhang, H., Cai, X., and Song, Y.: Characteristics of the

atmospheric boundary layer and its relation with $PM_{2.5}$ during haze episodes in winter in the North China Plain, Atmospheric Environment, 223, https://doi.org/10.1016/j.atmosenv.2020.117265, 2020.

Li, X.-B., Wang, D.-S., Lu, Q.-C., Peng, Z.-R., and Wang, Z.-Y.: Investigating vertical distribution patterns of lower tropospheric $PM_{2.5}$ using unmanned aerial vehicle measurements, Atmospheric Environment, 173, 62-71, https://doi.org/10.1016/j.atmosenv.2017.11.009, 2018.

Liu, C., Huang, J., Wang, Y., Tao, X., Hu, C., Deng, L., Xu, J., Xiao, H.-W., Luo, L., Xiao, H.-Y., and Xiao, W.: Vertical distribution of $PM_{2.5}$ and interactions with the atmospheric boundary layer during the development stage of a heavy haze pollution event, Science of the Total Environment, 704, https://doi.org/10.1016/j.scitotenv.2019.135329, 2020.

Liu, C., Chen, R., Sera, F., Vicedo-Cabrera, A. M., Guo, Y., Tong, S., Coelho, M. S. Z. S., Saldiva, P. H. N., Lavigne, E., Matus, P., Ortega, N. V., Garcia, S. O., Pascal, M., Stafoggia, M., Scortichini, M., Hashizume, M., Honda, Y., Hurtado-Diaz, M., Cruz, J., Nunes, B., Teixeira, J. P., Kim, H., Tobias, A., Iniguez, C., Forsberg, B., Astrom, C., Ragettli, M. S., Guo, Y.-L., Chen, B.-Y., Bell, M. L., Wright, C. Y., Scovronick, N., Garland, R. M., Milojevic, A., Kysely, J., Urban, A., Orru, H., Indermitte, E., Jaakkola, J. J. K., Ryti, N. R. I., Katsouyanni, K., Analitis, A., Zanobetti, A., Schwartz, J., Chen, J., Wu, T., Cohen, A., Gasparrini, A., and Kan, H.: Ambient Particulate Air Pollution and Daily Mortality in 652 Cities, New England Journal of Medicine, 381, 705-715, https://doi.org/10.1056/NEJMoa1817364, 2019.

Liu, H., Yuan, R., Mei, J., Sun, J., Liu, Q., and Wang, Y.: Scale Properties of Anisotropic and Isotropic Turbulence in the Urban Surface Layer, Boundary-Layer Meteorology, 165, 277-294, https://doi.org/10.1007/s10546-017-0272-z, 2017.

Ma, T., Duan, F., He, K., Qin, Y., Tong, D., Geng, G., Liu, X., Li, H., Yang, S., Ye, S., Xu, B., Zhang, Q., and Ma, Y.: Air pollution characteristics and their relationship with emissions and meteorology in the Yangtze River Delta region during 2014-2016, Journal of Environmental Sciences, 83, 8-20,

https://doi.org/10.1016/j.jes.2019.02.031, 2019.

Miao, Y., Li, J., Miao, S., Che, H., Wang, Y., Zhang, X., Zhu, R., and Liu, S.: Interaction Between Planetary Boundary Layer and $PM_{2.5}$ Pollution in Megacities in China: a Review, Current Pollution Reports, 5, 261-271, https://doi.org/10.1007/s40726-019-00124-5, 2019.

Mlawer, E. J., Taubman, S. J., Brown, P. D., Iacono, M. J., and Clough, S. A.: Radiative transfer for inhomogeneous atmospheres: RRTM, a validated correlated-k model for the longwave, Journal of Geophysical Research-Atmospheres, 102, 16663-16682, https://doi.org/10.1029/97jd00237, 1997.

Morrison, H., Thompson, G., and Tatarskii, V.: Impact of Cloud Microphysics on the Development of Trailing Stratiform Precipitation in a Simulated Squall Line: Comparison of One- and Two-Moment Schemes, Monthly Weather Review, 137, 991-1007, https://doi.org/10.1175/2008mwr2556.1, 2009.

Peng, Y., Wang, H., Li, Y., Liu, C., Zhao, T., Zhang, X., Gao, Z., Jiang, T., Che, H., and Zhang, M.: Evaluating the performance of two surface layer schemes for the momentum and heat exchange processes during severe haze pollution in Jing-Jin-Ji in eastern China, Atmospheric Chemistry and Physics, 18, 17421-17435, https://doi.org/10.5194/acp-18-17421-2018, 2018.

Pierce, A. M., Loria-Salazar, S. M., Holmes, H. A., and Gustin, M. S.: Investigating horizontal and vertical pollution gradients in the atmosphere associated with an urban location in complex terrain, Reno, Nevada, USA, Atmospheric Environment, 196, 103-117, https://doi.org/10.1016/j.atmosenv.2018.09.063, 2019.

Qian, Y., Gustafson, W. I., Jr., and Fast, J. D.: An investigation of the sub-grid variability of trace gases and aerosols for global climate modeling, Atmospheric Chemistry and Physics, 10, 6917-6946, https://doi.org/10.5194/acp-10-6917-2010, 2010.

Quan, J., Dou, Y., Zhao, X., Liu, Q., Sun, Z., Pan, Y., Jia, X., Cheng, Z., Ma, P., Su, J., Xin, J., and Liu, Y.: Regional atmospheric pollutant transport mechanisms over the North China Plain driven by topography and planetary boundary layer processes, Atmospheric Environment, 221, https://doi.org/10.1016/j.atmosenv.2019.117098,

1274 2020.

Ren, Y., Zhang, H., Wei, W., Cai, X., and Song, Y.: Determining the fluctuation of $PM_{2.5}$ mass concentration and its applicability to Monin-Obukhov similarity, Science of the Total Environment, 710, https://doi.org/10.1016/j.scitotenv.2019.136398, 2020.

Ren, Y., Zhang, H., Wei, W., Cai, X., Song, Y., and Kang, L.: A study on atmospheric turbulence structure and intermittency during heavy haze pollution in the Beijing area, Science China-Earth Sciences, 62, 2058-2068, https://doi.org/10.1007/s11430-019-9451-0, 2019a.

Ren, Y., Zhang, H., Wei, W., Wu, B., Cai, X., and Song, Y.: Effects of turbulence structure and urbanization on the heavy haze pollution process, Atmospheric Chemistry and Physics, 19, 1041-1057, https://doi.org/10.5194/acp-19-1041-2019, 2019b.

Ren, Y., Zhang, H., Zhang, X., Li, Q., Cai, X., Song, Y., Kang, L., and Zhu, T.: Temporal and spatial characteristics of turbulent transfer and diffusion coefficient of $PM_{2.5}$, Science of the Total Environment, 782, https://doi.org/10.1016/j.scitotenv.2021.146804, 2021.

Riccobono, F., Schobesberger, S., Scott, C. E., Dommen, J., Ortega, I. K., Rondo, L., Almeida, J., Amorim, A., Bianchi, F., Breitenlechner, M., David, A., Downard, A., Dunne, E. M., Duplissy, J., Ehrhart, S., Flagan, R. C., Franchin, A., Hansel, A., Junninen, H., Kajos, M., Keskinen, H., Kupc, A., Kuerten, A., Kvashin, A. N., Laaksonen, A., Lehtipalo, K., Makhmutov, V., Mathot, S., Nieminen, T., Onnela, A., Petaja, T., Praplan, A. P., Santos, F. D., Schallhart, S., Seinfeld, J. H., Sipila, M., Spracklen, D. V., Stozhkov, Y., Stratmann, F., Tome, A., Tsagkogeorgas, G., Vaattovaara, P., Viisanen, Y., Vrtala, A., Wagner, P. E., Weingartner, E., Wex, H., Wimmer, D., Carslaw, K. S., Curtius, J., Donahue, N. M., Kirkby, J., Kulmala, M., Worsnop, D. R., and Baltensperger, U.: Oxidation Products of Biogenic Emissions Contribute to Nucleation of Atmospheric Particles, Science, 344, 717-721, https://doi.org/10.1126/science.1243527, 2014.

Skamarock, W. C., Klemp, J. B., Dudhia, J., Gill, D. O., and Powers, J. G.: A Description of the Advanced Research WRF Version 3, NCAR Technical Note

NCAR/TN-475+STR. June 2008. Mesoscale and Microscale Meteorology Division. National Center for Atmospheric Research. Boulder, 475, 2008.

Stull, R. B.: An Introduction to Boundary Layer Meteorology, An Introduction to Boundary Layer Meteorology1988.

Sun, T., Che, H., Qi, B., Wang, Y., Dong, Y., Xia, X., Wang, H., Gui, K., Zheng, Y., Zhao, H., Ma, Q., Du, R., and Zhang, X.: Aerosol optical characteristics and their vertical distributions under enhanced haze pollution events: effect of the regional transport of different aerosol types over eastern China, Atmospheric Chemistry and Physics, 18, 2949-2971, https://doi.org/10.5194/acp-18-2949-2018, 2018.

Sun, Y., Song, T., Tang, G., and Wang, Y.: The vertical distribution of $PM_{2.5}$ and boundary-layer structure during summer haze in Beijing, Atmospheric Environment, 74, 413-421, https://doi.org/10.1016/j.atmosenv.2013.03.011, 2013.

Tao, H., Xing, J., Zhou, H., Pleim, J., Ran, L., Chang, X., Wang, S., Chen, F., Zheng, H., and Li, J.: Impacts of improved modeling resolution on the simulation of meteorology, air quality, and human exposure to $PM_{2.5}$, O_3 in Beijing, China, Journal of Cleaner Production, 243, https://doi.org/10.1016/j.jclepro.2019.118574, 2020.

Tuccella, P., Curci, G., Visconti, G., Bessagnet, B., Menut, L., and Park, R. J.: Modeling of gas and aerosol with WRF-Chem over Europe: Evaluation and sensitivity study, Journal of Geophysical Research-Atmospheres, 117, https://doi.org/10.1029/2011jd016302, 2012.

Wang, H., Peng, Y., Zhang, X., Liu, H., Zhang, M., Che, H., Cheng, Y., and Zheng, Y.: Contributions to the explosive growth of $PM_{2.5}$ mass due to aerosol-radiation feedback and decrease in turbulent diffusion during a red alert heavy haze in Beijing-Tianjin-Hebei, China, Atmospheric Chemistry and Physics, 18, 17717-17733, https://doi.org/10.5194/acp-18-17717-2018, 2018.

Wei, W., Zhang, H., Cai, X., Song, Y., Bian, Y., Xiao, K., and Zhang, H.: Influence of Intermittent Turbulence on Air Pollution and Its Dispersion in Winter 2016/2017 over Beijing, China, Journal of Meteorological Research, 34, 176-188, https://doi.org/10.1007/s13351-020-9128-4, 2020.

Wei, W., Zhang, H., Wu, B., Huang, Y., Cai, X., Song, Y., and Li, J.: Intermittent turbulence contributes to vertical dispersion of PM$_{2.5}$ in the North China Plain: cases from Tianjin, Atmospheric Chemistry and Physics, 18, 12953-12967, https://doi.org/10.5194/acp-18-12953-2018, 2018.

Wiedinmyer, C., Akagi, S. K., Yokelson, R. J., Emmons, L. K., Al-Saadi, J. A., Orlando, J. J., and Soja, A. J.: The Fire INventory from NCAR (FINN): a high resolution global model to estimate the emissions from open burning, Geoscientific Model Development, 4, 625-641, https://doi.org/10.5194/gmd-4-625-2011, 2011.

Wild, O., Zhu, X., and Prather, M. J.: Fast-j: Accurate simulation of in- and below-cloud photolysis in tropospheric chemical models, Journal of Atmospheric Chemistry, 37, 245-282, https://doi.org/10.1023/a:1006415919030, 2000.

WRAP – Western Regional Air Partnership: 2002 Fire Emission Inventory for the WRAP Region – Phase II, Project No.178-6, available at: http://www.wrapair.org/forums/fejf/tasks/FEJFtask7PhaseII.html (last access: 30 September 2021), 2005.

Wu, H., Li, Z., Li, H., Luo, K., Wang, Y., Yan, P., Hu, F., Zhang, F., Sun, Y., Shang, D., Liang, C., Zhang, D., Wei, J., Wu, T., Jin, X., Fan, X., Cribb, M., Fischer, M. L., Kulmala, M., and Petaja, T.: The impact of the atmospheric turbulence-development tendency on new particle formation: a common finding on three continents, National Science Review, 8, https://doi.org/10.1093/nsr/nwaa157, 2021.

Xu, J., Yan, F., Xie, Y., Wang, F., Wu, J., and Fu, Q.: Impact of meteorological conditions on a nine-day particulate matter pollution event observed in December 2013, Shanghai, China, Particuology, 20, 69-79, https://doi.org/10.1016/j.partic.2014.09.001, 2015.

Ye, X., Song, Y., Cai, X., and Zhang, H.: Study on the synoptic flow patterns and boundary layer process of the severe haze events over the North China Plain in January 2013, Atmospheric Environment, 124, 129-145, https://doi.org/10.1016/j.atmosenv.2015.06.011, 2016.

Yin, P., Brauer, M., Cohen, A., Burnett, R. T., Liu, J., Liu, Y., Liang, R., Wang, W., Qi,

J., Wang, L., and Zhou, M.: Long-term Fine Particulate Matter Exposure and Nonaccidental and Cause-specific Mortality in a Large National Cohort of Chinese Men, Environmental Health Perspectives, 125, https://doi.org/10.1289/ehp1673, 2017.

Yuan, R., Luo, T., Sun, J., Liu, H., Fu, Y., and Wang, Z.: A new method for estimating aerosol mass flux in the urban surface layer using LAS technology, Atmospheric Measurement Techniques, 9, 1925-1937, https://doi.org/10.5194/amt-9-1925-2016, 2016.

Zaveri, R. A. and Peters, L. K.: A new lumped structure photochemical mechanism for large-scale applications, Journal of Geophysical Research-Atmospheres, 104, 30387-30415, https://doi.org/10.1029/1999jd900876, 1999.

Zaveri, R. A., Easter, R. C., Fast, J. D., and Peters, L. K.: Model for Simulating Aerosol Interactions and Chemistry (MOSAIC), Journal of Geophysical Research-Atmospheres, 113, https://doi.org/10.1029/2007jd008782, 2008.

Zhang, H., Zhang, X., Li, Q., Cai, X., Fan, S., Song, Y., Hu, F., Che, H., Quan, J., Kang, L., and Zhu, T.: Research progress on estimation of atmospheric boundary layer height, Acta Meteorologica Sinica, 78, 522-536, 2020.

Zhang, L., Zhang, H., Li, Q., Cai, X., and Song, Y.: Vertical dispersion mechanism of long-range transported dust in Beijing: Effects of atmospheric turbulence, Atmospheric Research, 269, https://doi.org/10.1016/j.atmosres.2022.106033, 2022.

Zhang, L., Sun, J. Y., Shen, X. J., Zhang, Y. M., Che, H., Ma, Q. L., Zhang, Y. W., Zhang, X. Y., and Ogren, J. A.: Observations of relative humidity effects on aerosol light scattering in the Yangtze River Delta of China, Atmospheric Chemistry and Physics, 15, 8439-8454, https://doi.org/10.5194/acp-15-8439-2015, 2015a.

Zhang, M., Zhao, C., Yang, Y., Du, Q., Shen, Y., Lin, S., Gu, D., Su, W., and Liu, C.: Modeling sensitivities of BVOCs to different versions of MEGAN emission schemes in WRF-Chem (v3.6) and its impacts over eastern China, Geoscientific Model Development, 14, 6155-6175, https://doi.org/10.5194/gmd-14-6155-2021, 2021.

Zhang, R., Wang, G., Guo, S., Zarnora, M. L., Ying, Q., Lin, Y., Wang, W., Hu, M., and Wang, Y.: Formation of Urban Fine Particulate Matter, Chemical Reviews, 115, 3803-3855, https://doi.org/10.1021/acs.chemrev.5b00067, 2015b.

Zhang, Z., Xu, X., Qiao, L., Gong, D., Kim, S.-J., Wang, Y., and Mao, R.: Numerical simulations of the effects of regional topography on haze pollution in Beijing, Scientific Reports, 8, https://doi.org/10.1038/s41598-018-23880-8, 2018.

Zhao, C., Liu, X., Leung, L. R., and Hagos, S.: Radiative impact of mineral dust on monsoon precipitation variability over West Africa, Atmospheric Chemistry and Physics, 11, 1879-1893, https://doi.org/10.5194/acp-11-1879-2011, 2011.

Zhao, C., Leung, L. R., Easter, R., Hand, J., and Avise, J.: Characterization of speciated aerosol direct radiative forcing over California, Journal of Geophysical Research-Atmospheres, 118, 2372-2388, https://doi.org/10.1029/2012jd018364, 2013a.

Zhao, C., Li, Y., Zhang, F., Sun, Y., and Wang, P.: Growth rates of fine aerosol particles at a site near Beijing in June 2013, Advances in Atmospheric Sciences, 35, 209-217, https://doi.org/10.1007/s00376-017-7069-3, 2018.

Zhao, C., Chen, S., Leung, L. R., Qian, Y., Kok, J. F., Zaveri, R. A., and Huang, J.: Uncertainty in modeling dust mass balance and radiative forcing from size parameterization, Atmospheric Chemistry and Physics, 13, 10733-10753, https://doi.org/10.5194/acp-13-10733-2013, 2013b.

Zhao, C., Hu, Z., Qian, Y., Leung, L. R., Huang, J., Huang, M., Jin, J., Flanner, M. G., Zhang, R., Wang, H., Yan, H., Lu, Z., and Streets, D. G.: Simulating black carbon and dust and their radiative forcing in seasonal snow: a case study over North China with field campaign measurements, Atmospheric Chemistry and Physics, 14, 11475-11491, https://doi.org/10.5194/acp-14-11475-2014, 2014.

Zhao, C., Huang, M., Fast, J. D., Berg, L. K., Qian, Y., Guenther, A., Gu, D., Shrivastava, M., Liu, Y., Walters, S., Pfister, G., Jin, J., Shilling, J. E., and Warneke, C.: Sensitivity of biogenic volatile organic compounds to land surface parameterizations and vegetation distributions in California, Geoscientific Model Development, 9, 1959-1976, https://doi.org/10.5194/gmd-9-1959-2016, 2016.

Zhao, X. J., Zhao, P. S., Xu, J., Meng, W., Pu, W. W., Dong, F., He, D., and Shi, Q. F.:

Analysis of a winter regional haze event and its formation mechanism in the North China Plain, Atmospheric Chemistry and Physics, 13, 5685-5696, https://doi.org/10.5194/acp-13-5685-2013, 2013c.

Zhong, J., Zhang, X., Dong, Y., Wang, Y., Liu, C., Wang, J., Zhang, Y., and Che, H.: Feedback effects of boundary-layer meteorological factors on cumulative explosive growth of $PM_{2.5}$ during winter heavy pollution episodes in Beijing from 2013 to 2016, Atmospheric Chemistry and Physics, 18, 247-258, https://doi.org/10.5194/acp-18-247-2018, 2018.

1464

Table 1 WRF-Chem model configuration

Horizontal resolution	25 km & 5 km & 1 km
Domain size	140 x 105 & 250 x 250 & 150 x 150
Simulation period	5 March to 21 March 2019
Gas-phase chemistry scheme	SAPRC99 mechanism
Radiation scheme	Fast-J
PBL scheme	YSU scheme
Microphysics scheme	Morrison two-moment scheme
Land surface scheme	Noah land-surface scheme
Cumulus scheme	Kain-Fritsch (25 km grid only)
Surface layer scheme	Revised MM5 Monin-Obukhov scheme
Longwave radiation scheme	RRTMG scheme
Shortwave radiation scheme	RRTMG scheme

1465
1466
1467
1468
1469
1470
1471
1472
1473
1474
1475
1476
1477
1478
1479
1480
1481
1482
1483
1484
1485
1486
1487
1488
1489
1490
1491
1492
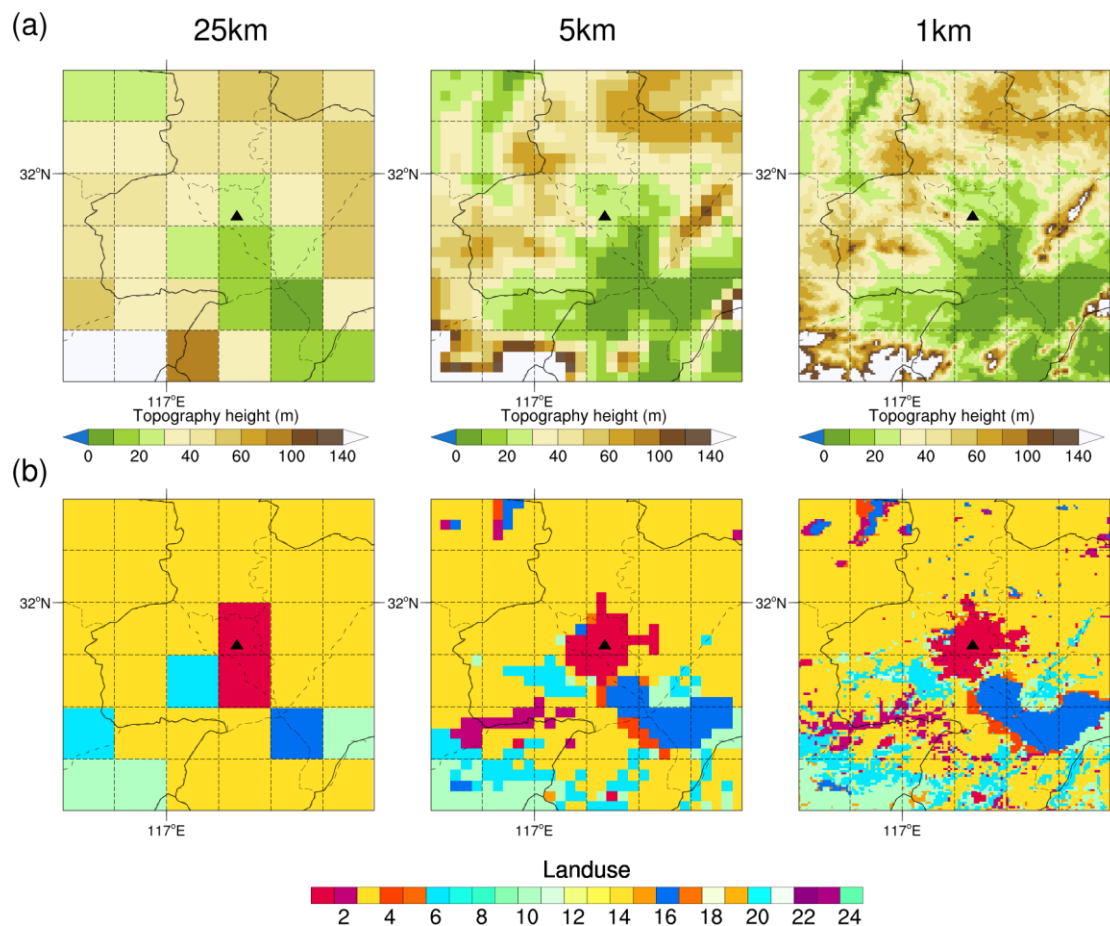
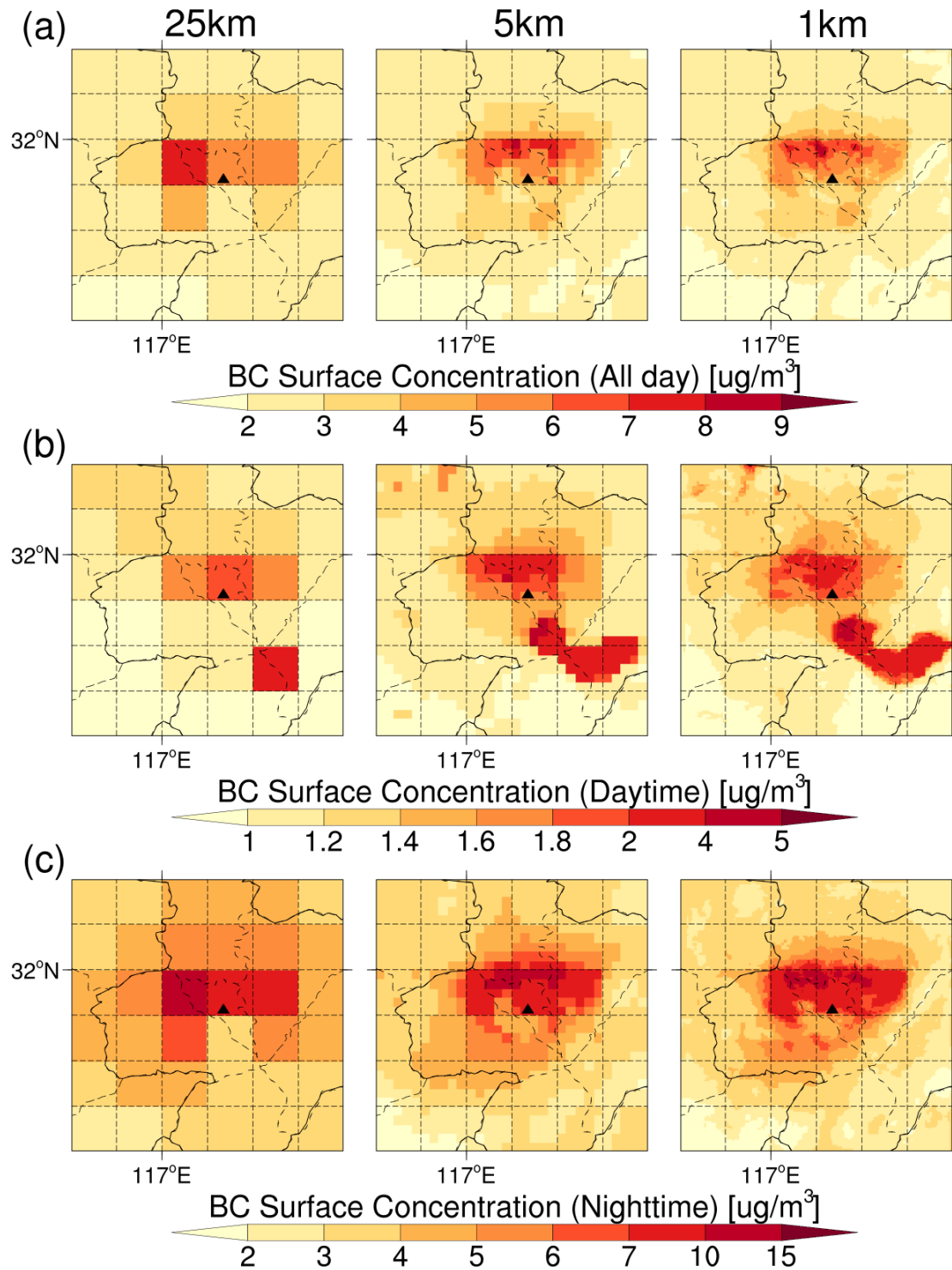**Figure 1.** (a) The terrain height (m) in the study area for 25-km (left), 5-km (middle), and 1-km (right) resolution simulations, respectively; (b) Spatial distribution of land use types in the study area for 25-km (left), 5-km (middle), and 1-km (right) resolution simulations, respectively. The solid black triangle indicates the location of the USTC site.
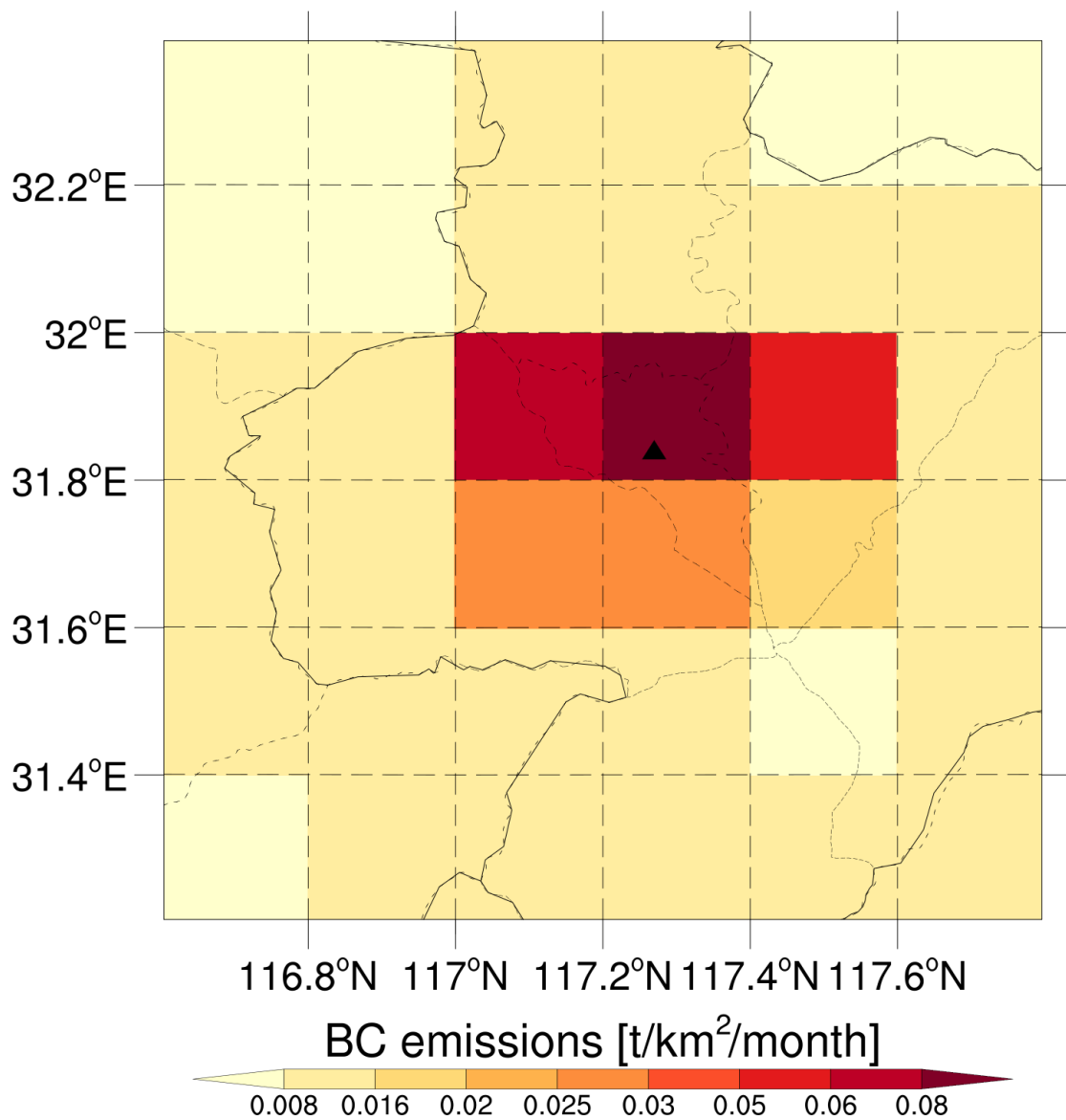
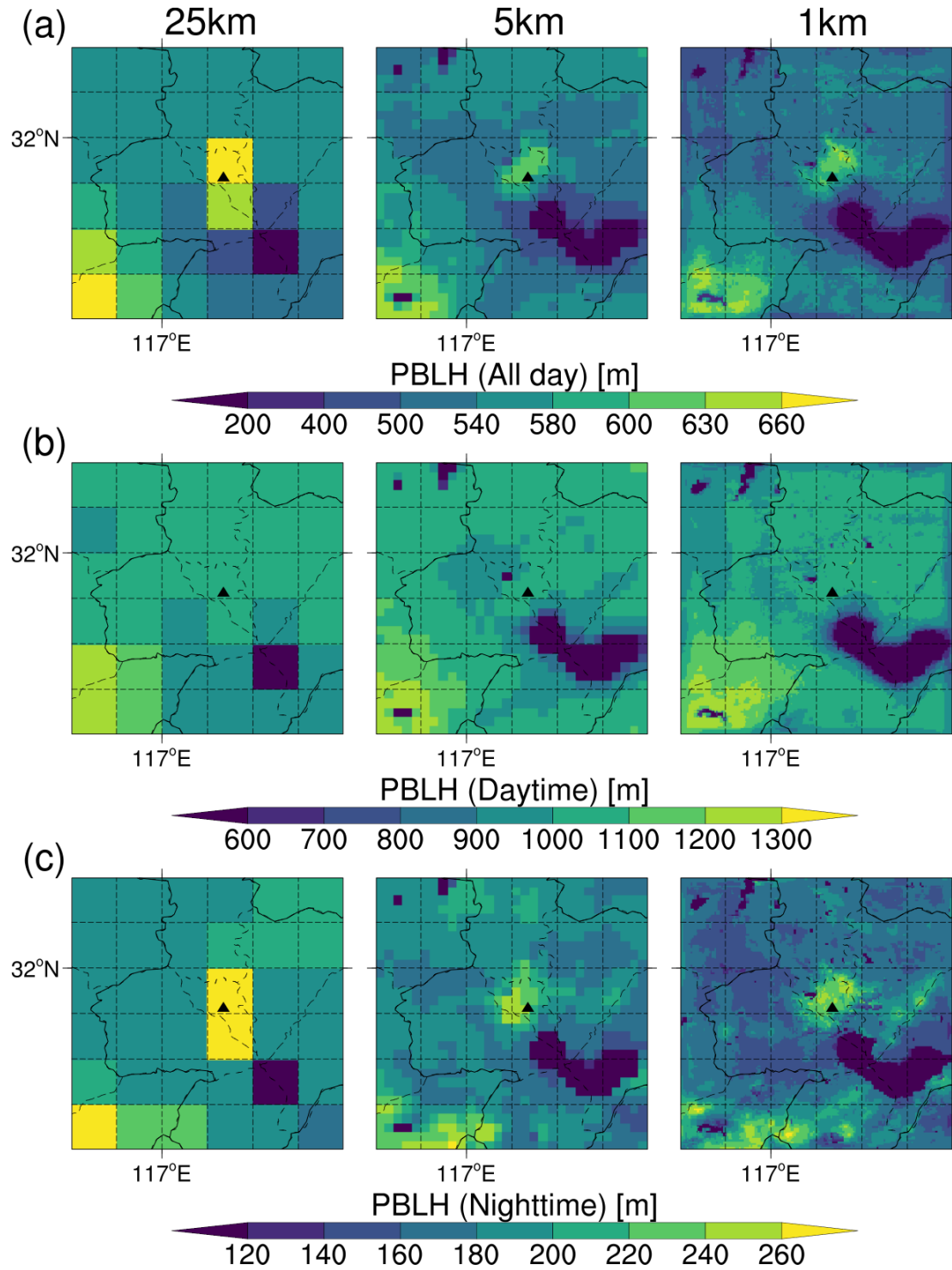**Figure 2.** Spatial distribution of BC emissions in the study area. The solid black triangle indicates the location of the USTC site.
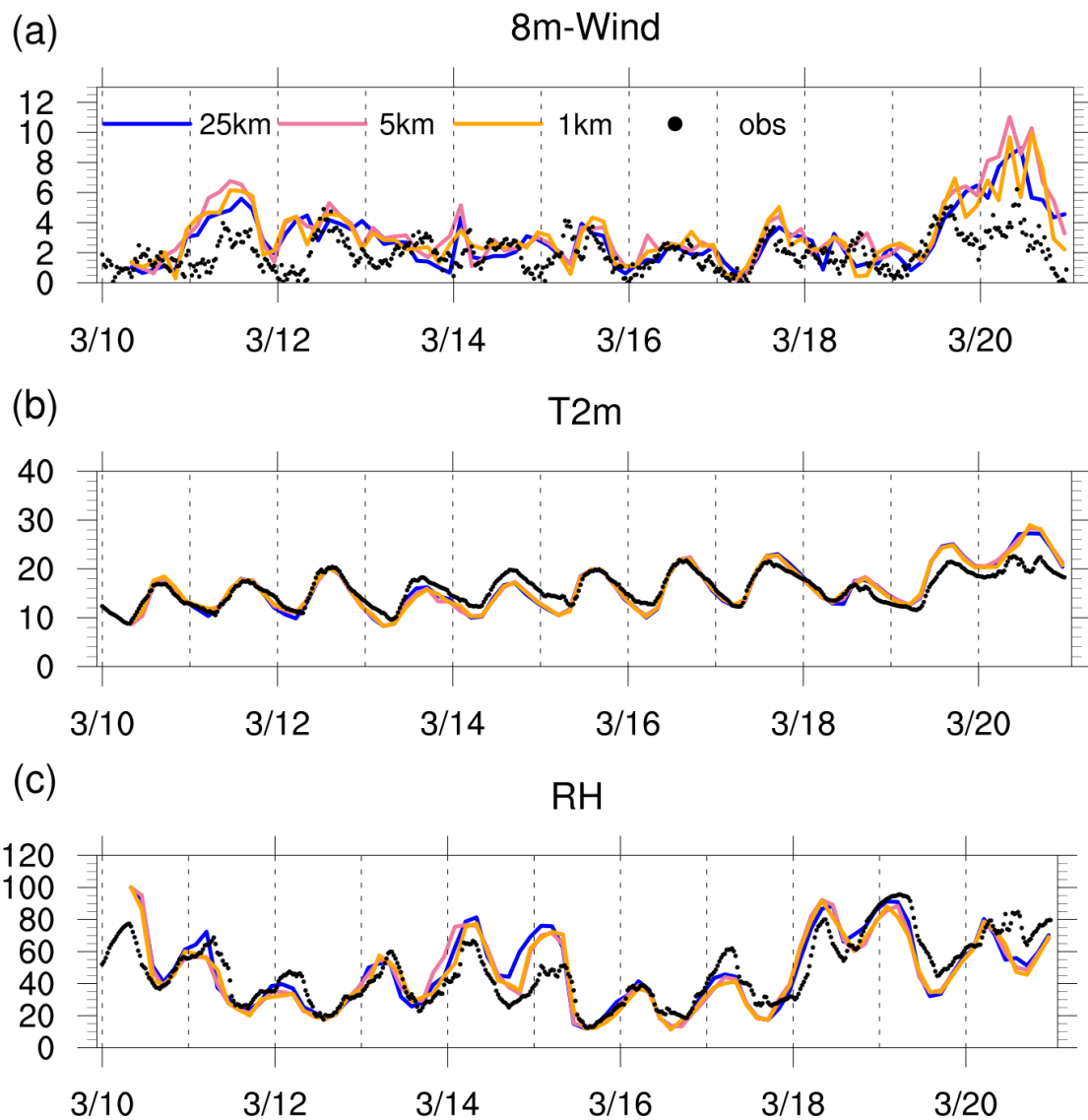
Figure 3. Time series at USTC meteorological tower observation site of observed

(black dot) and simulated wind speed at 8 m (top, unit: m s^{-1}), temperature at 2 m

(middle, unit: °C), and relative humidity (bottom, unit: %) for 25-km (solid blue line)

resolution, 5-km (solid pink line) resolution, and 1-km (solid orange line) resolution,

respectively.

Figure 4. Spatial distribution of the BC surface concentration in the study area for 25-km (left), 5-km (middle), and 1-km (right) resolution simulations of the whole day (top), the daytime (middle), and the nighttime (bottom), respectively. The solid black triangle indicates the location of the USTC site.

1540

1541
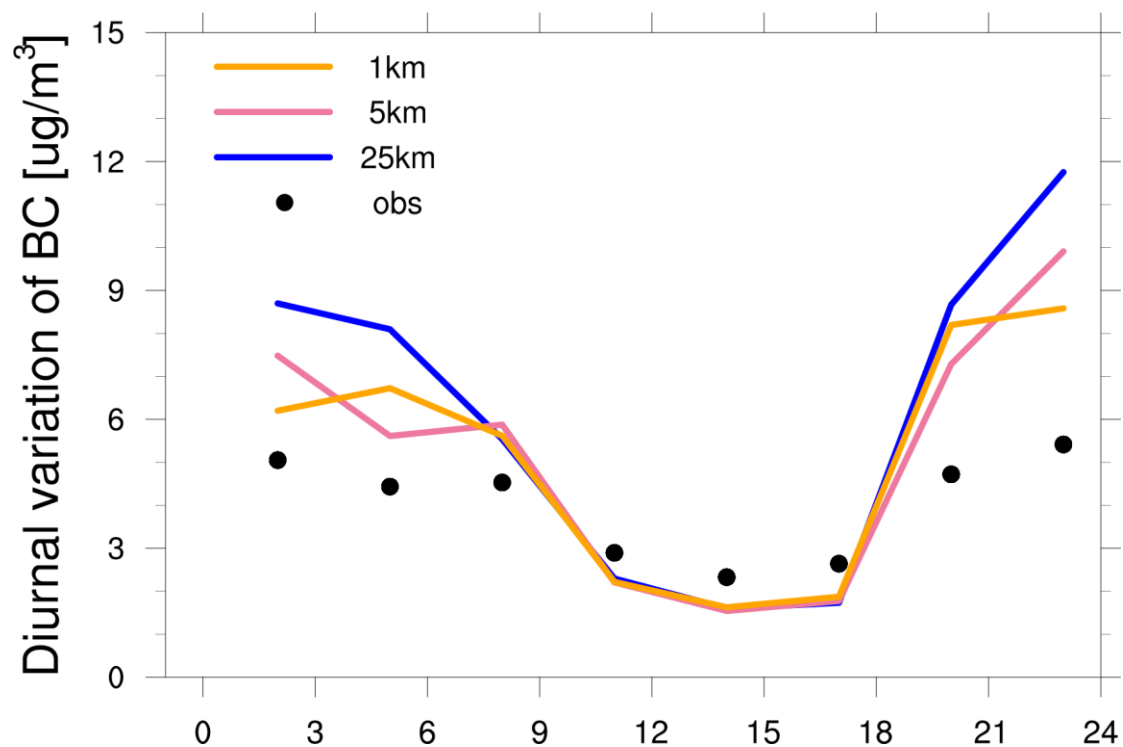
Figure 5. Diurnal variation of BC surface concentrations within 24 h averaged over

the USTC site during the study period for 25-km (solid blue line), 5-km (solid pink

line), and 1-km (solid orange line) resolution simulations and observations (black

dot). Both the simulated results and observations are sampled at the model output

frequency, i.e., 3-hourly.

1547

1548

1549

1550

1551

1552

1553

1554

1555

1556

1557

1558

Figure 6. Spatial distribution of the PBL height in the study area for 25-km (left), 5-km (middle), and 1-km (right) resolution simulations of the whole day (top), the daytime (middle), and the nighttime (bottom), respectively. The solid black triangle indicates the location of the USTC site.
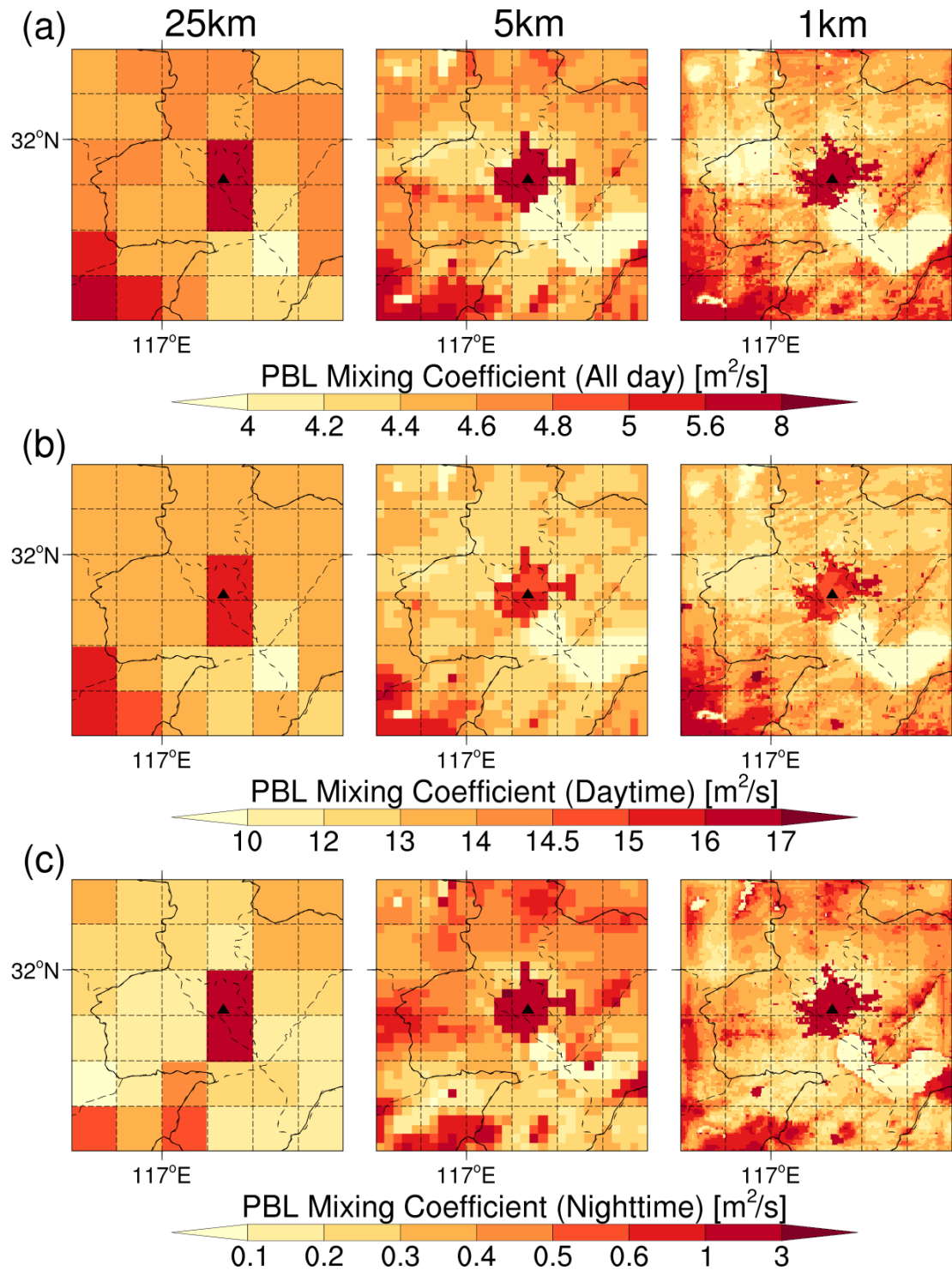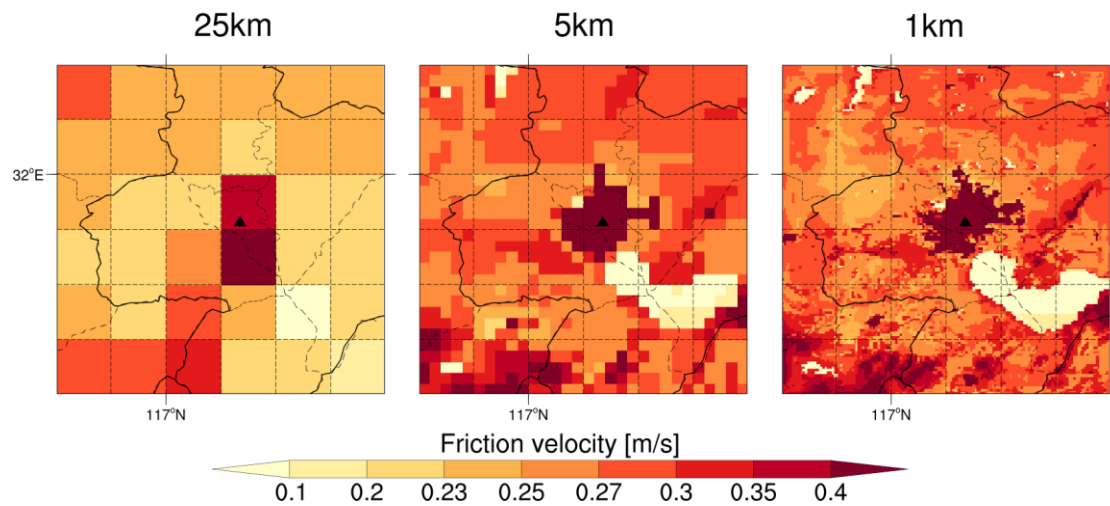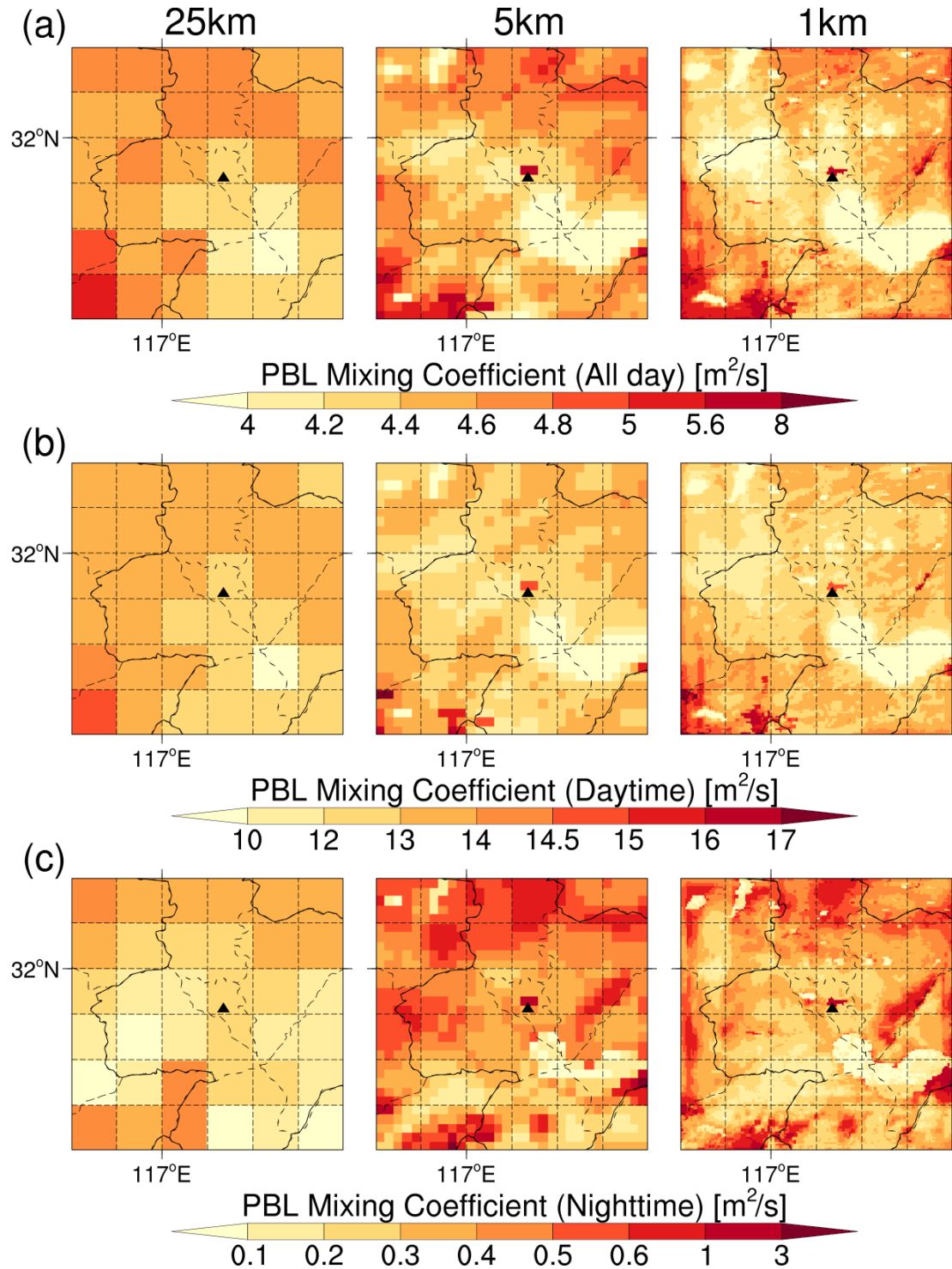
Figure 7. Spatial distribution of PBL mixing coefficients in the study area for 25-km (left), 5-km (middle), and 1-km (right) resolution simulations of the whole day (top), the daytime (middle), and the nighttime (bottom), respectively. The solid black triangle indicates the location of the USTC site.
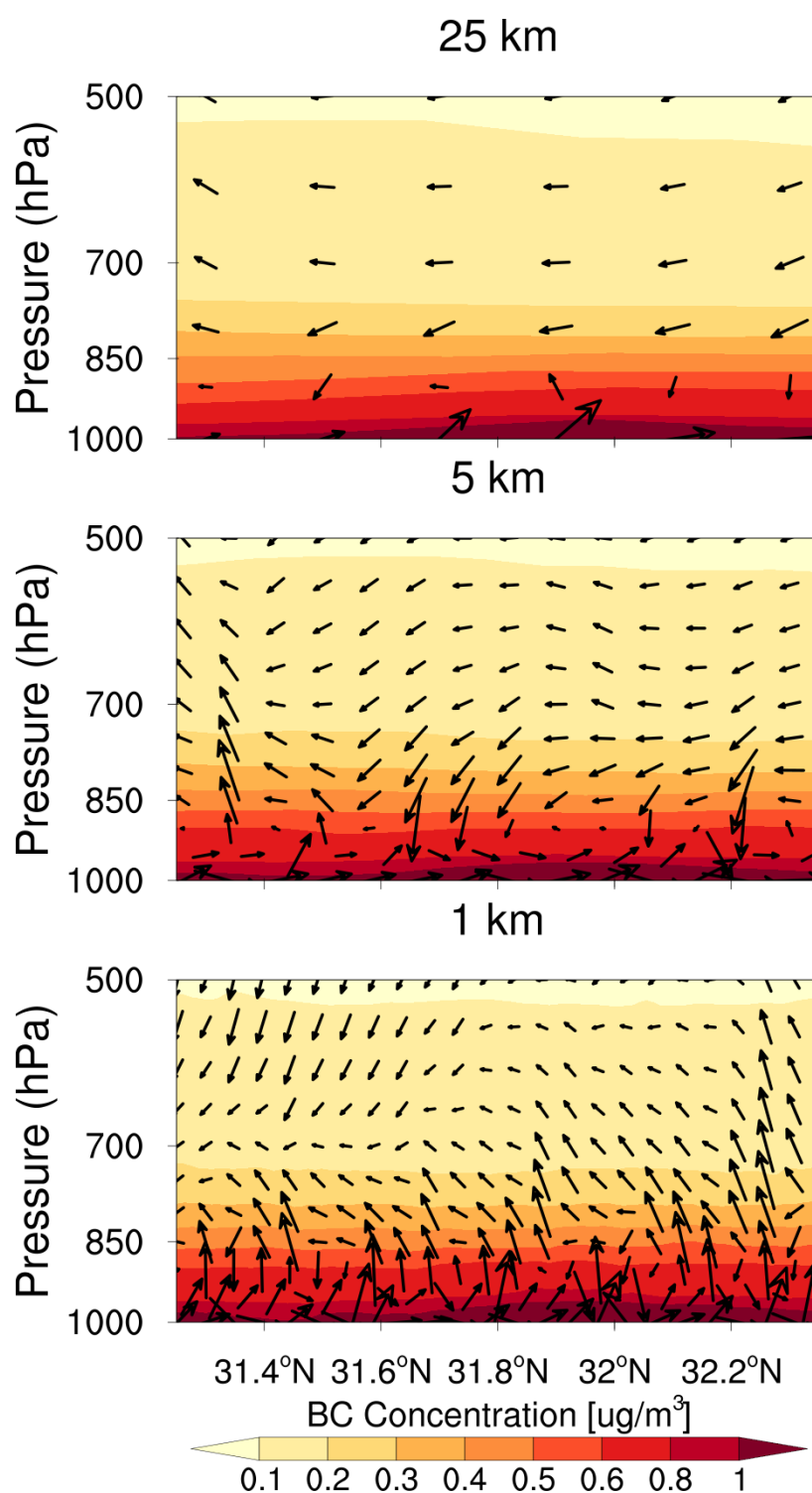
Figure 8. The latitude-pressure cross section of BC concentrations and wind speed flux along the USTC site for 25-km (top), 5-km (middle), and 1-km (bottom) resolution simulations of the whole day, respectively. Vector arrows are the combination of wind speed fluxes v and w, with the vertical wind speed flux being multiplied by 100 for visibility. The shaded contours represent BC concentrations at each pressure level.

Figure 9. Spatial distribution of friction velocity in the study area for 25-km (left), 5-km (middle), and 1-km (right) resolution simulations of the whole day, respectively. The solid black triangle indicates the location of the USTC site.

Figure 10. Spatial distribution of PBL mixing coefficients in the study area for 25-km (left), 5-km (middle), and 1-km (right) resolution simulations of the whole day (top), the daytime (middle), and the nighttime (bottom), respectively. The solid black triangle indicates the location of the USTC site. The simulation results are from the three sensitivity experiments.
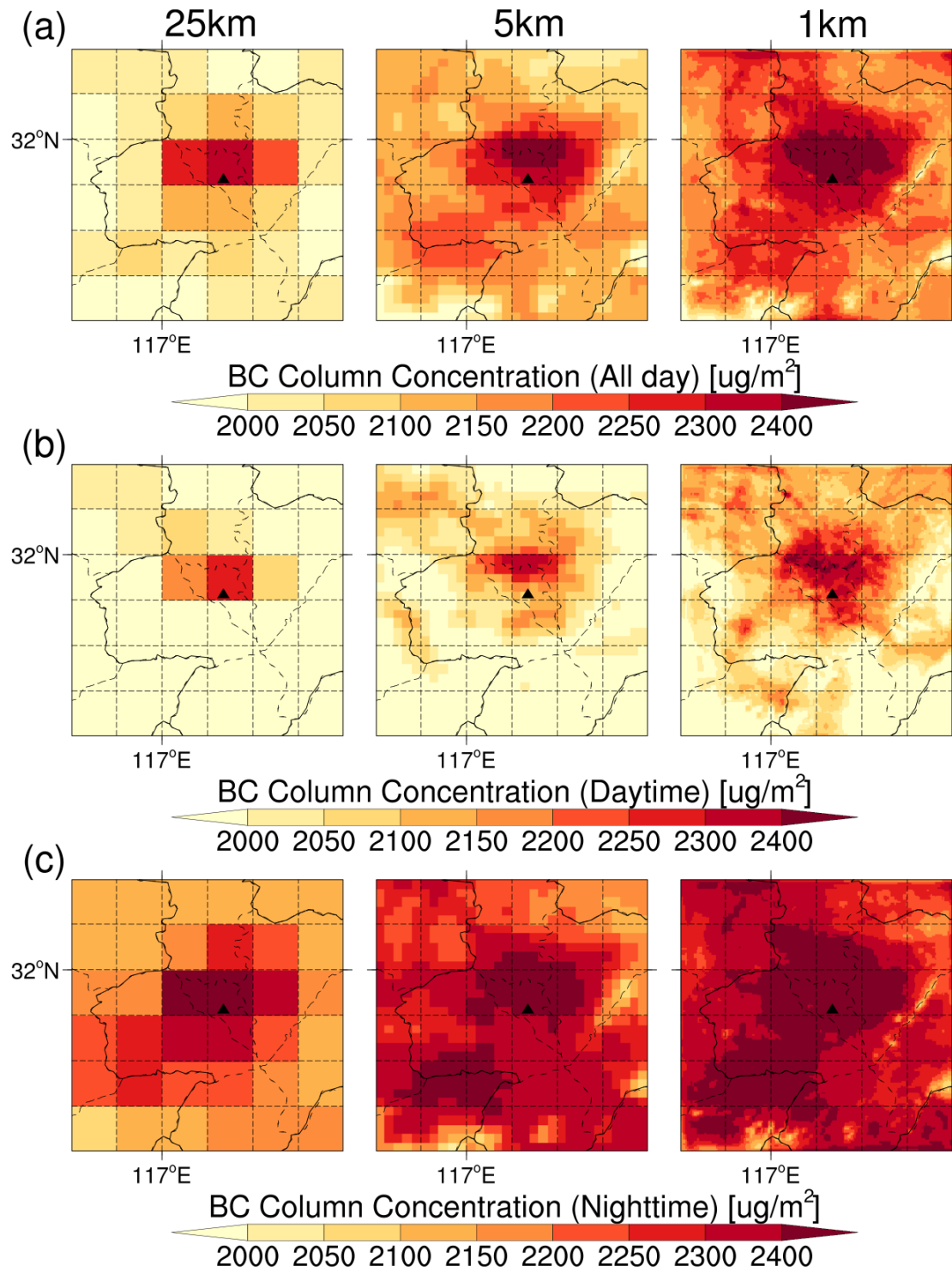
Figure 11. Spatial distribution of the BC column concentration in the study area for 25-km (left), 5-km (middle), and 1-km (right) resolution simulations of the whole day (top), the daytime (middle), and the nighttime (bottom), respectively. The solid black triangle indicates the location of the USTC site.
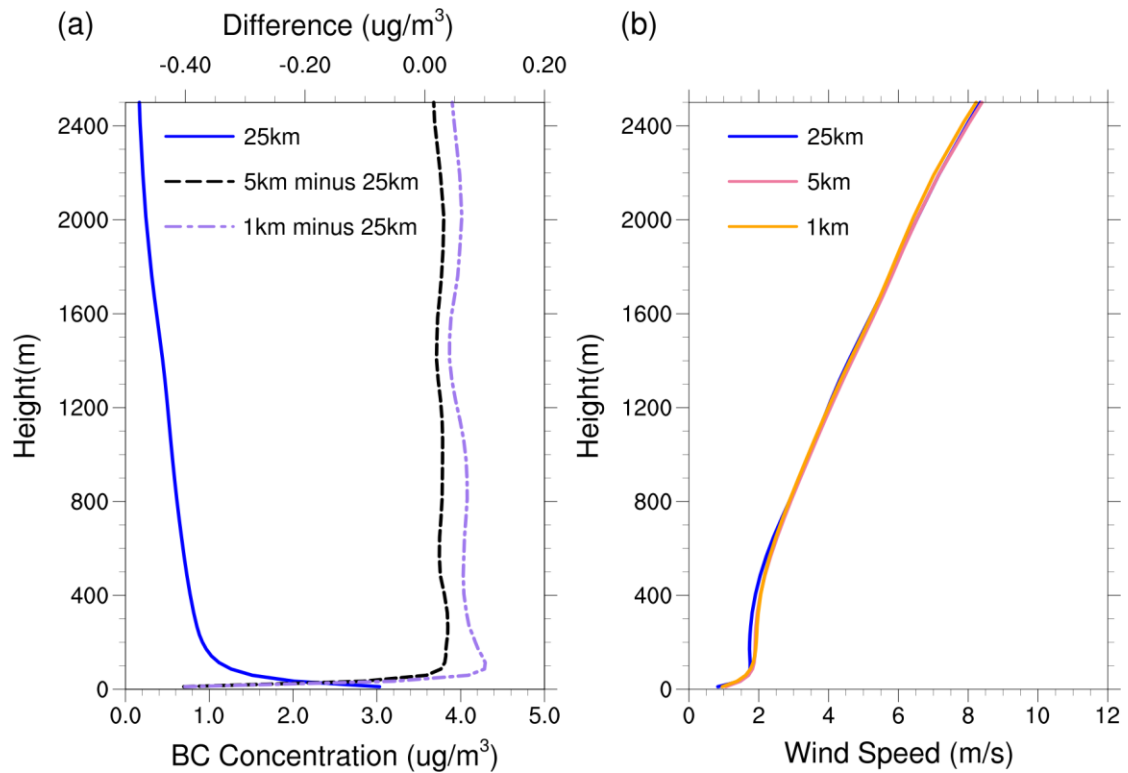
Figure 12. (a) Vertical profiles of BC concentrations simulated at 25-km resolution (solid blue line), the difference between 5-km and 25-km resolutions (dashed black line), and the difference between 1-km and 25-km resolutions (dashed purple line) averaged over the study area for the whole day, respectively. (b) Vertical profiles of wind speed simulated at 25-km resolution (solid blue line), 5-km resolution (solid pink line), and 1-km resolution (solid orange line) averaged over the study area for the whole day, respectively.
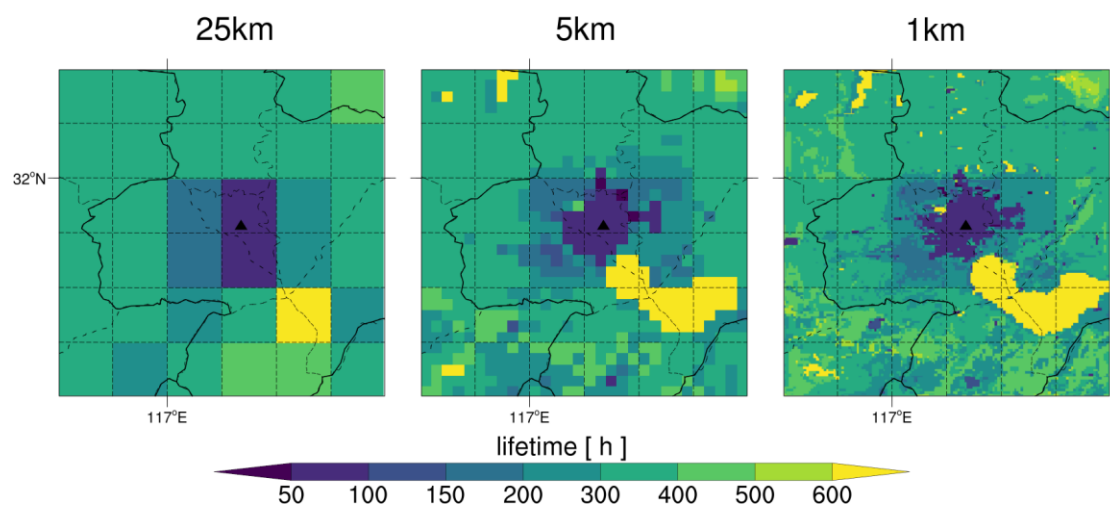
Figure 13. Spatial distribution of the lifetime in the study area for 25-km (left), 5-km (middle), and 1-km (right) resolution simulations of the whole day, respectively. The solid black triangle indicates the location of the USTC site.